university of groningen

faculty of science and engineering

The Study of [Th/Eu] as a Cosmic Chronometer

Ainun Azhari

university of groningen / faculty of science and engineering

University of Groningen

The Study of [Th/Eu] as a Cosmic Chronometer

Master's Thesis

To fulfill the requirements for the degree of
Master of Science in Astronomy
at the University of Groningen under the supervision of
Dr. Tadafumi Matsuno
and
Prof. dr. Eline Tolstoy

Ainun Azhari (s4646371)

July 4, 2023

”Progress looks more like a rough staircase than a smooth upward curve. Failures are the building blocks for your staircase to success. The more times you fail, the higher the staircase will be.”

someone once told me this, right when I was about to give up

Abstract

Stellar age is a fundamental parameter in astronomy, and most age-determination methods are model-dependent. This currently has been alleviated by asteroseismology, allowing more precise age determination through seismic masses. However, this method is rather expensive to perform for a large number of stars, and so it is desirable to have some alternative methods to derive stellar age precisely and less expensively.

In this thesis, I investigate the use of [Th/Eu] as a chronometer. I derive [Eu/Fe] and [Th/Fe] abundances to study the reliability of [Th/Eu] abundance ratio to determine stellar age. I also explore the use of the Th II line at 5989 $\AA$ to derive reliable Th abundance.

I determine the abundance ratios of [Eu/Fe], [Th/Fe], and [Th/Eu] using high-resolution spectra and spectral synthesis code Turbospectrum. For this purpose, I use the Eu II line at 6645 $\AA$ which is commonly used and widely studied to obtain reliable Eu abundance. For Th abundance determination, I use the Th II line at 5989 $\AA$. This line is less troubled by blending compared to the more commonly used line the more commonly used Th II line at 4019 $\AA$, which is not available in the spectra.

I found that the stars in my sample follow different trends for [Eu/Fe] and [Th/Fe] against [Fe/H], despite the common assumption that Th and Eu should follow the same abundance evolution since both are produced in r-process nucleosynthesis. I also found that [Th/Fe] is significantly higher than what was observed for main-sequence stars in literature, while [Eu/H] has more similar values. I found only weak correlations between the abundance ratios with stellar age, with [Th/Fe] showing a decreasing trend while [Eu/Fe] shows an increasing trend. This might point to a possible difference in their productions and enrichment history. Future research could help alleviate the issues encountered in this study by observing the more widely studied Th II line at 4019 $\AA$ for the stars in our sample to cross-check the Th II abundance measurements.

This approach could be useful to determine stellar age for a large number of stars in the Milky Way, as an alternative to asteroseismology which requires long and continuous photometric observations. Improving the lab measurements of the atomic transitions producing the absorption lines and taking into account all the transitions of other elements in the close vicinity of the Th II lines under study would also help to improve the robustness of these results.

1 Introduction

Stellar age is one of the most important parameters in making sense of the properties of the Milky Way and all other galaxies. It is used as an input to model galaxy formation, the age-metallicity relation, and the star formation rate (Lebreton & Goupil, 2014). Therefore, it is of great concern to determine the stellar age as precisely as possible. However, determining stellar age is not straightforward, as in most cases, the methods available are model-dependent as they need some knowledge of physical processes in stars (Lebreton et al., 2014). For example, the commonly applied method of using stellar isochrones is highly dependent on stellar evolution models, which have various uncertainties in and of themselves. Our limited knowledge of what exactly happens in the interior of the stars as they evolve poses a barrier to modeling stellar evolution precisely (Lebreton & Goupil, 2014). This problem has been alleviated by the emergence of asteroseismology, from exoplanet-search missions and observations of long-term light curves of stars from which frequencies of internal stellar oscillation are derived (Lebreton & Goupil, 2014). This has allowed the determination of more precise stellar masses and ages. Determining the oscillation frequencies requires long, continuous, and accurate photometric observations (Bedding et al., 2010), thus it is expensive to perform for a large number of stars. Therefore, it is desirable to also have some other methods to determine stellar age precisely and less expensively.

In this thesis, I present nucleochronology as a possible method of stellar age determination. This requires the abundance ratio of two elements to be measured, one subject to radioactive decay with a half-life time comparable to the age of the Universe and one stable, [Th/Eu]. Thorium is exclusively produced by the r-process, while Eu has dominant r-process abundance (Bisterzo et al., 2014, only a tiny contribution from the s-process, up to 6% in the Sun). The most stable isotope of Th is ^{232}Th, which decays with a half-life of 1.45×10^{10} years. This long decay time is comparable to the age of the universe, which makes Th suitable as a cosmic chronometer. Europium is a stable element that does not undergo decay. Assuming that Th and Eu are produced together, the depletion of the Th abundance compared to Eu should indicate how much time has passed since the elements were formed. With the assumption that the elements formed shortly before the star was formed, this could serve as a means to determine stellar age (Cowan et al., 1997; Butcher, 1987).

In Subsection 1.1 I summarise the basic principles of asteroseismology, how it can be used to determine stellar age, and the NASA Kepler mission providing asteroseismic data. After summarizing the basic principles of nucleochronology in Subsection 1.2, I will explain the production of elements in Subsection 1.3. I will review the formation of absorption lines and how they are used to determine stellar abundances are summarised in Subsection 1.4. Finally, the motivation of this study is described in Subsection 1.5.

1.1 Asteroseismology

Asteroseismology is the study of the internal oscillation of stars. Asteroseismic observations extract information on the frequencies, amplitudes, and phases of internal oscillations through observed photometric variations on the stellar surface (Aerts et al., 2010). Asteroseismology thus relies on observing precise light curves, which show a periodical change in the star's flux due to ongoing internal oscillations and other physical processes, such as convection and mixing. The properties of the oscillations are sensitive to the global properties of stars, such as mass, radius, and internal structure. This is how asteroseismology plays a role in stellar mass determination, and subsequently, in stellar age derivation. The actual application is described in the next subsections.

1.1.1 Internal Oscillations of Stars

The internal oscillation of stars is analogous to the sound waves created by musical instruments, as described in Aerts et al. (2010). In the case of a star, the core acts as the node, and the surface as the anti-node of the oscillation. As three-dimensional spherical objects, stars oscillate in three orthogonal directions that are best defined in spherical coordinates (r, θ, ϕ). In the case of a star, r is the distance from the center of the star, θ is the angular distance from the stellar pole (also called the colatitude since latitude is measured from the equator), and ϕ is the longitude. Stellar oscillations consist of various modes which are characterized by three quantum numbers n, l, and m. These represent the overtone of the nodes (the number of radial nodes), the azimuthal order of the mode (the number of surface nodes that are lines of longitudes), and the degree of the mode (the number of surface nodes). One simple example is the fundamental radial mode ($l = 0$), where the center of the star acts as the node and the surface as the anti-node, making the star pulsate inward and outward. Higher degree modes penetrate shallower regions from the surface compared to lower degree modes, and this difference in depths reached makes asteroseismology a powerful tool to probe the interior of stars.

In stars, the oscillations are driven by pressure, and this is called the p-mode of the oscillations, where pressure acts as the restoring force. In addition, gravity also drives pulsation with the buoyancy of the gas acting as the restoring force, called the g-mode of the oscillation. Both modes are sensitive to different depths of the stellar interior, where p-modes are mostly sensitive to the conditions on the surface, while g-modes are mostly sensitive to the conditions at the core.

Concerning the observational aspects of asteroseismology, the oscillation of stars implements itself through an excess power in the time series (Silva Aguirre & Serenelli, 2016). This is described by two parameters, the average large frequency separation $\langle \Delta\nu \rangle$ and the frequency of maximum power $\nu_{\max}$, which we will describe in Section 1.1.2. The large separation is a function of the sound speed $c(r)$ and the radius of the star, which is then related to the mass of the star, through the relation:

$$\Delta\nu = \left(2 \int_0^R \frac{1}{c(r)} \, dr \right)^{-1}, \tag{1}$$

where R is the radius of the star.

1.1.2 Stellar Age Determination

There are several methods to determine stellar age from the oscillation properties in asteroseismology. One of them is to obtain the star's large frequency separation $\Delta\nu$ and the oscillation modes' maximum frequency $\nu_{\max}$, and use a scaling relation to determine the mass (Silva Aguirre & Serenelli, 2016). The mass can then be used to derive the age of the star using an isochrone. Compared to other mass determination methods, asteroseismology is relatively model-independent (Serenelli et al., 2021).

Low-mass stars show oscillations in p-mode and are thus called solar-like oscillators due to the similarity in the restoring force in these stars with that in the sun. This includes main sequence stars, red giants, AGB stars, and red clump stars. The oscillation of this type of star is characterized by $\Delta\nu$ and ν_{max}, which are correlated.

Figure 1 shows the tight correlation between $\Delta\nu$ and $\nu_{\max}$ for red giants. This correlation follows a power-law in the form of $\Delta\nu = (0.263 \pm 0.009)\mu\text{Hz}(\nu_{\max}/\mu\text{Hz})^{0.772\pm0.005}$ (Stello et al., 2009). This power-law relation is advantageous in analyzing seismic data, as $\Delta\nu$ can easily be determined given a value of $\nu_{\max}$ (Stello et al., 2009). It can also be expressed as a scaling relation with that of the Sun, $\Delta\nu = \Delta\nu_{\odot}(\nu_{\max}/\nu_{\max\odot})^{0.784\pm0.003}$ (Hekker et al., 2009). The scaling relation shows that these two parameters scale in a uniform way despite the stellar evolution (Hekker et al., 2009). The fact that $\Delta\nu$

[b]

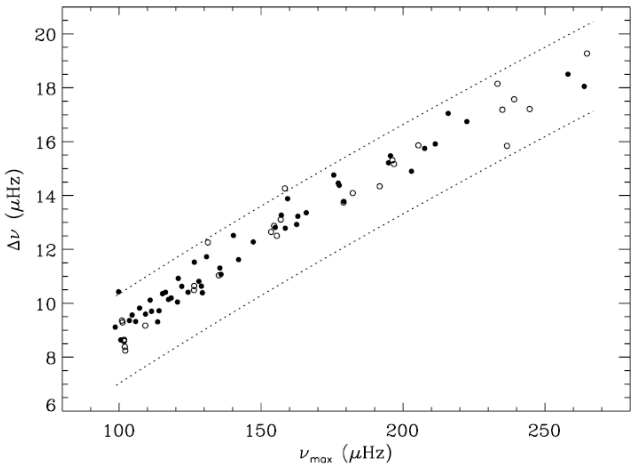

Figure 1: The relation between $\Delta\nu$ and ν_{max} for 78 red giants, filled circles showing stars selected for further observation in the Kepler mission. Dashed lines show parameter space covered by $\sim 80\%$ of the observation. Adapted from Bedding et al. (2010).

and ν_{max} are correlated shows that the oscillation frequencies happen at regular intervals in these stars (Hekker et al., 2009). This is an important property that is useful in using $\Delta\nu$ and ν_{max} as observables to derive seismic mass.

The large separation $\Delta\nu$ is observationally detected from the periodic feature that is visible in the power spectrum. The frequency of maximum power ν_{max} is obtained from the power distribution of the oscillation, which shows a maximum at a certain frequency (see Figure 2). The oscillation modes have different amplitudes for different frequencies, so we can see it as a distribution of power as a function of frequency. This results from the balance between excitation and damping.

The parameters $\Delta\nu$ and ν_{max} are related to the density and temperature of the stars (Serenelli et al. (2021) and references therein):

$$\Delta\nu \propto \sqrt{\rho} \equiv \sqrt{M/R^3} \tag{2}$$

$$\nu_{max} \equiv g/\sqrt{T_{eff}} = GM/(R^2\sqrt{T_{eff}}) \tag{3}$$

solving these equations for R and M, then dividing them by the solar values gives a scaling relation to determine radius and mass as a function of $\Delta\nu$ and ν_{max}. If T_{eff} is known, then radius and mass can be determined through a scaling relation of the form:

$$\frac{R}{R_\odot} = \left(\frac{\nu_{max}}{\nu_{max,\odot}}\right)\left(\frac{\Delta\nu}{\Delta\nu_\odot}\right)^{-2}\left(\frac{T_{eff}}{T_\odot}\right)^{1/2} \tag{4}$$

$$\frac{M}{M_\odot} = \left(\frac{\nu_{max}}{\nu_{max,\odot}}\right)^{3}\left(\frac{\Delta\nu}{\Delta\nu_\odot}\right)^{-4}\left(\frac{T_{eff}}{T_\odot}\right)^{3/2}. \tag{5}$$

1.1.3 NASA Kepler Mission

In this thesis, we made use of stellar age derived from seismic data obtained from observations made with the Kepler satellite. NASA's Kepler mission, which was launched on March 6, 2009, was designed to detect Earth-sized planets through the transit-photometry method and characterize them

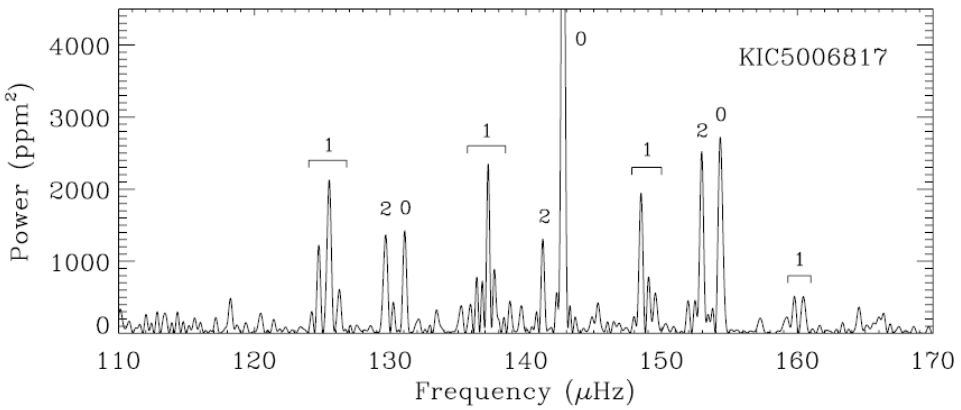

Figure 2: The power spectrum of the star KIC 5006817 shows the peak of maximum power at frequencies of $110-170\mu$Hz. The label on each peak denotes the degree l. Adapted from Bedding et al. (2010).

(Koch et al., 2010). The targets to be observed were listed in the Kepler Input Catalog (KIC), which includes the stellar parameters of the target candidates (Gilliland et al., 2010). These targets were selected based on their radii to observe stars that are the most probable to host Earth-like planets. This consisted mostly of solar-like stars, although the mission also observed a number of red giants for the purpose of distant reference for astrometry (Gilliland et al., 2010). These stars were aimed to be used to study a small change in position due to proper motion, variability, and the presence of an unseen companion (Monet et al., 2010). The magnitude of this small change is then applied to the whole Kepler sample, which is important to pinpoint the accurate positions of the stars.

There are several important features of the mission that are suited for asteroseismic observations. These include a stable platform that allows long observations, and a wide field to cover many stars over a wide range in stellar brightness with high precision photometry (Gilliland et al., 2010). This is particularly important for red-giant stars that require long ($>\sim 30$ days) and uninterrupted time series to resolve the oscillations (Bedding et al., 2010). The observed data come in the form of power spectra of the oscillations (see Figure 2) and the light curve of the transits. The power spectrum displays various modes of oscillation at different frequencies, which are mixed with background signals. It is visible in the figure that each mode exhibits different power, with maximum power at a certain frequency $\nu_{\rm max}$. By fitting the observed power spectra with a global model, the background signals and the oscillation parameters $\Delta\nu$ and $\nu_{\rm max}$ can be identified (**?**). The model could also be used to find the patterns of the radial and nonradial oscillation, along with the mode degree. After $\Delta\nu$ and $\nu_{\rm max}$ are determined from the model fitting, the stellar mass and radius are estimated, e.g., by using a grid of stellar models, or by using scaling relations as explained above.

1.2 Nucleochronology

Nucleochronology is a method of stellar age determination based on the radioactive decay of elements. Assuming that the half-life time and the initial abundance of an element are known, the present abundance can be used to infer the amount of time that has passed since the element was produced. This practically gives a means to determine the stellar age by assuming that the elements were produced shortly before star formation, or by assuming a chemical evolution model. This method has an advantage of being independent of stellar evolution models compared to other age determination methods. It relies solely on the assumed initial abundance and the half-life time of the element un-

der study. The elements used for this purpose are often called cosmic chronometers, which could be various combinations of heavy elements.

There are several combinations of elements that have been studied as cosmic chronometers, e.g., [U/Th], [Th/Eu], and [Th/Dy]. In principle, the closer the two elements are in masses, the more reliable the chronometer should be (Cayrel et al., 2001). Compared to nuclei with larger mass differences, neighboring nuclei have almost identical atomic parameters and thus are not highly sensitive to the r-process model uncertainties. These similarities of the neighboring nuclei make them less prone to systematic uncertainties (Frebel et al., 2007; Goriely & Clerbaux, 1999). Therefore, the abundance ratio of elements that are close together in masses, such as [U/Th], could be used as a more reliable age estimator. According to Roederer et al. (2009), the chronometer of [Th/r] (r denotes any r-process element) is in third place in terms of the strength to predict stellar ages following [U/r] and [U/Th].

Using a chronometer as a means of determining stellar age should be done very carefully. The initial abundance of elements should be estimated precisely through a theoretical prediction. This might vary between stars, e.g., the initial abundance of the Sun would be different from that of very metal-poor stars (Honda et al., 2004). Therefore, a good understanding of the r-process through chemical evolution models is needed to accurately estimate the stellar age. This could be alleviated, for example, by using several pairs of [Th/r] chronometers, employing different r-process elements (Honda et al., 2004).

1.3 Nucleosynthesis in the universe

As we focus on deriving elemental abundance in this thesis, we will discuss briefly how elements form. It has been well-established that nucleosynthesis takes place in stars (Burbidge et al., 1957). Although all stars on the main sequence burn H into He, the degree to which stellar nucleosynthesis can proceed depends on the initial stellar mass. Low-mass and intermediate-mass stars can produce elements up until C and O. On the other hand, massive stars can form elements until they form Fe and Fe-peak elements (Holmbeck et al., 2023).

Iron cannot burn into any heavier elements due to the high Coulomb barrier (Holmbeck et al., 2023), putting a stopping point for stellar nucleosynthesis. However, the existence of elements heavier than Fe in stellar spectra creates the requirement for another nucleosynthetic process to produce them. They are considered to be produced by neutron-capture reactions. There are two types of neutron-capture processes, s-process (the slow neutron capture process) and the r-process (the rapid neutron capture process). While s-process takes place in intermediate-mass stars at the AGB phase, the r-process site is believed to occur in violent events such as supernova explosions and neutron star mergers. This is described in more detail in Section 1.3.1.

1.3.1 *s*- and *r*-process Elements

In order to use elemental abundance ratios for nucleochronology, it is important to have a good understanding of the neutron capture processes. The r-process is of special importance since Th is exclusively produced by this process and Eu is also mainly produced by it. The neutron-capture processes are responsible for producing elements with the proton number $Z \geq 30$. In particular, super-heavy elements such as U and Th are exclusively produced by the r-process. Most of the elements found in stellar abundances are the result of mixing between s- and r-process productions.

There are different conditions that allow the occurrence of the s- and r-process nucleosynthesis. In general, both processes require a high neutron density. The environmental condition of the nucle-

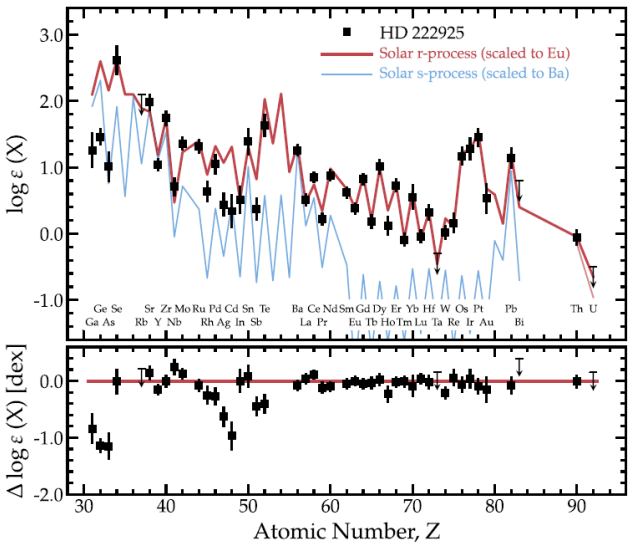

Figure 3: The universal abundance pattern for the r-process elements, shown in the star HD222925 as compared to the Sun. Shown in the top panel are the first, second, and third peaks of the neutron capture elemental abundance. The bottom panel shows the difference between the r-process abundance of HD 222925 and the solar residual. Adapted from Roederer et al. (2022).

osynthesis site affects the rate of the neutron capture reaction:

$$ {}^{A}_{Z}X + n \rightarrow {}^{A+1}_{Z}X. \tag{6} $$

In the s-process, the neutron capture rate is slower than the β^- decay rate, and vice versa for the r-process. This creates different pathways for both processes, as illustrated in Figure 4. This figure shows how nuclei are created in the s-process and r-process, going to the right (higher neutron number) as neutrons are captured until a nucleus with a short β^- decay lifetime is reached. At this branching point, the process proceeds diagonally to the upper left direction (higher proton number, lower neutron number) and continues to the right direction again, and so forth. This results in different end products of both processes, as some elements at the branching points might or might not be produced depending on what goes faster between the neutron capture and the β^- decay.

While the s-process is believed to take place in low- and intermediate-mass AGB stars (Arcones & Thielemann, 2023), the site(s) of the r-process is still under debate (Cowan et al., 2021). There are various sites that have been proposed as the r-process site throughout the years, such as core-collapse supernovae (CCSNe), hypernovae, neutron star-neutron star/black hole (NS-NS/BH) mergers. Wanajo et al. (2018) showed that neutron star mergers can achieve the conditions needed for the r-process nucleosynthesis. Other proposed sites include the post-merger accretion disk and tidally-stripped ejecta, and magnetorotational-driven supernovae (see Eichler et al. (2019); Hansen et al. (2014); Wehmeyer et al. (2015) for review).

The end result of the r-process depends on the astrophysical conditions under which it takes place, such as entropy, temperature, and density, along with the elements present as seed nuclei. A higher neutron density would increase the chance of producing more heavy nuclei through a stronger r-process, even at the same temperature and density (Holmbeck et al., 2023).

The observed elemental abundances of r-process elements across stars tend to show similarity, leading to the term ”the universality” of r-process (see Figure 3). It is visible in the upper panel of the figure that the abundance pattern of the star HD 222925 follows that of the Sun, also shown by

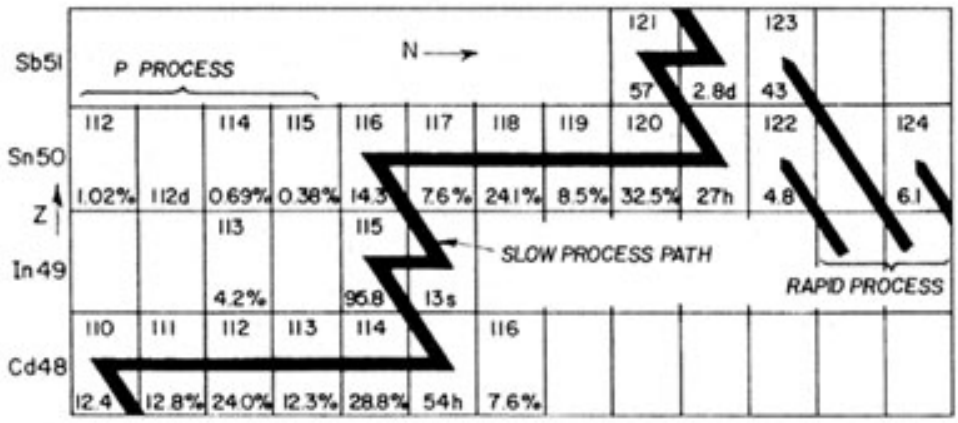

Figure 4: The schematic s- and r-process pathways create different final abundances of nuclei, denoted by the mass number on top of the boxes, percentage abundance for the stable isotopes and β^- decay lifetime for the unstable isotopes at the bottom of the boxes. Adapted from Pagel (2009).

the zero difference in the lower panel. Some deviations from zero may present in some stars for certain elements due to chemical peculiarity, but most elements would follow the universal pattern. This fact would be useful for nucleochronology, as the scaled abundance for any star could easily be calculated relative to a standard star, e.g., the Sun. There are stars that show an overabundance of actinides (e.g., Th) compared to the lanthanides (e.g., Eu), which later are called the actinide-boost stars. This poses a problem to the r-process universality. It is still unclear whether this is caused by different astrophysical conditions of one r-process site or different r-process sites altogether (Eichler et al., 2019).

1.4 Line absorption in stellar spectra

To precisely determine abundance from stellar spectra, it is important to understand how lines form and what affects their profiles in the spectra. Spectral lines are formed when there are enough absorbing particles in the stellar atmosphere (Gray, 1992). Spectral lines are often broadened by a number of causes, such as microturbulence, which refers to small-scale mass motion of order smaller than a unit of optical depth, causing an effect similar to the thermal Doppler broadening. The large-scale turbulent motions in the atmosphere cause the so-called macroturbulence. In addition, instrumental broadening is also important when dealing with observed stellar spectra. It is common to represent all broadening effects with one broadening parameter $v_{\rm broad}$ (Jofré et al., 2019).

The shape and strength of absorption lines depend on various conditions in the stellar atmosphere (Gray, 1992), e.g., the temperature, pressure, radiation, velocity of the gas, and in some cases, the magnetic field present in the star. The oscillator strength of the transition and the abundance of the absorbers also play a role in creating the line profile (Gray, 1992). With an increasing abundance of the absorber, the line would grow in three sequential ways, i.e., it would grow deeper up to a maximum point, after which it would become saturated, and then the wings would start to grow wider in the case of very strong lines. It is also important to note that the change in the other elements' abundance might also affect the line of interest through line blending. Variation only in the abundance of the element of interest would surely increase the strength of the line, but the effect of the variation of the remaining elements' abundance might lower the effect such that the growth would be less significant. These effects of abundance on the line profiles underlie the reason why absorption lines can be used to

determine abundance in the stellar photosphere.

1.4.1 Abundance Determination

Abundance determination is typically carried out in one of two different ways. The first is the EW method, using the curve of growth, which relates directly the abundance of an element to the observed equivalent width of the absorption lines. The second is spectral synthesis, which involves calculating spectra, including all lines within the chosen wavelength interval, and finding the abundances that match the observed spectrum. The abundance is highly dependent on physical variables and atomic constants, the most important of which are temperature and oscillator strength. It is in fact the uncertainty in the lab measurements of oscillator strength that often limit the precision of abundance determination. A differential approach is often done for stars with similar temperature and surface gravity, assuming that both have a similar curve of growth. In this way, the effect of errors on oscillator strength is canceled out.

There are advantages and disadvantages to both synthesis and EW methods. Both methods require a lengthy procedure. To create a curve of growth plot, the EW variation of each line of each element has to be calculated individually, and if there is blending the abundance will likely be overestimated. The spectral synthesis method also requires the creation of many synthetic spectra for a range of abundances for each element under study. However, spectral synthesis holds an advantage over the EW method, as synthesis is especially useful when the line under study is very weak or severely blended, for example in the case of cool stars or when the rotational broadening is large. In this method, the abundance and all broadenings are adjusted until the synthesized spectrum matches the observed one. Synthesis is also the only option when spectra are heavily blended, and/or contaminated by molecules.

To perform abundance analysis, a model atmosphere is needed to calculate the continuum in the synthetic spectra. There are several simplifications commonly used in creating model atmospheres, such as one-dimensional geometry (either adopting plane parallel approximation or assuming a spherical symmetry) and hydrostatic equilibrium. The excitation and ionization of the gas are often described in terms of thermodynamic equilibrium, and this is applied to a small volume of space in the photosphere. This approach is called the local thermodynamic equilibrium (LTE), where the photosphere is characterized by a uniform temperature at each depth. Within this approach, the model atmosphere then consists of temperature and pressure as functions of optical depth, where outer layers are of lower temperature. This information is used to compute a synthetic spectral energy distribution, which is done by calculating the flux at each frequency assuming a source function as a function of optical depth.

There are several types of errors from different sources in abundance determination. One is photon noise, which is defined by the signal-to-noise ratio (S/N). When the signal is not significantly higher than the noise, the abundance derived in the spectra is less reliable as there might be contamination from photon noise. There are also uncertainties due to the atmospheric parameters, the effects of which vary for neutral and ionized lines. Another is the systematic error that comes from the method employed. For example, 1D LTE model is an approximation often used in modeling stellar photosphere that affects the calculation of the transitions happening in the atmosphere. Any deviation from this approximation in real stellar photosphere changes the line profiles caused by those transitions. This error could be minimized by comparing the 1D LTE calculations with the publicly available 3D NLTE calculations and making a correction. This effect is more prominent in metal-poor stars. One is the instrumental error, which comes from any defect in the instrument used in the observation. This can be determined by comparing spectra obtained with different instruments or observing a calibrated

star of known properties repeatedly with different S/N ratios.

There are several ways to improve the precision of abundance determination. Using a standard calibrated star to calculate differential abundance will reduce the effects of NLTE, and reduce uncertainty in continuum placement as it should be at the same position for two stars of the same type. Using more lines could also improve abundance measurement, though it is not always possible. Some elements do not have many lines present in stellar spectra, or the lines are not in good condition. In order to have a reliable abundance determination, the lines used should not be blended or too weak.

The final abundance, A_X is commonly presented as the solar scaled value [X/H], or [X/Fe]:

$$[X/H] = A_X - A_{X,\odot} \tag{7}$$

$$= \log \frac{N_X}{N_H} - \log \frac{N_{X,\odot}}{N_{H,\odot}} \tag{8}$$

$$[X/Fe] = [X/H] - [Fe/H], \tag{9}$$

where

$$A_X = \log \frac{N_X}{N_H} + 12 \tag{10}$$

$$[Fe/H] = A_{Fe} - A_{Fe,\odot}. \tag{11}$$

1.5 This study

From the background information described above, I now proceed to the research carried out in this thesis. In this thesis, I aim to determine the abundance of Eu and Th using spectroscopic data to obtain the abundance ratio [Th/Eu]. I also explore the reliability of the Th II line at 5989 $\AA$ to derive Th abundance. The use of this line to derive the [Th/Eu] abundance ratio would be advantageous for determining stellar ages using nucleochronology. This approach can be applied to a large number of stars as an alternative to asteroseismology.

For this purpose, I analyze a sample of red giant branch stars in the Kepler field, which have reliable stellar masses and ages determined from asteroseismology. The stars also have archive high-resolution spectra, which gives us the advantage of having both spectroscopic and seismic data for the sample. This allows us to check the relation between the abundance ratio and the stellar age.

When analyzing the Th II line at 5989 $\AA$, there are several cautions we need to take care of regarding the absorption lines nearby. We have to carefully take into account the presence of Si I and Nd II lines in the close vicinity of the Th II line in order to derive the Th abundance precisely, as we will describe in Section 4. The weakness of the line also limits the number of stars with analyzable line, as we will describe in Section 2.

We divide the rest of this thesis as follows. In Section 2, we further describe the spectroscopic data we use and how we select the final sample. In Section 3 we describe the methods used, including specific adjustments that need to be taken into account concerning our sample. The results are presented in Section 4, and the possible interpretation and future prospects are discussed in Section 5. Finally, the conclusions are given in Section 6.

2 Creating a Sample

Our initial sample consists of high-resolution spectra obtained by Takeda & Tajitsu (2015), and additional data by Takeda et al. (2016), from now on dubbed the Takeda sample. This sample consists of 90 stars in the Kepler field, for which masses are robustly determined using the satellite's seismic data by Mosser et al. (2012), and ages determined using the seismic masses and isochrone method by Takeda et al. (2016).

2.1 Data

We used the archive spectra obtained by Takeda & Tajitsu (2015), who observed 42 stars using High Dispersion Spectrograph on Subaru Telescope, with a resolving power of $R \simeq 80000$ covering the wavelength range of $\sim$ 5100 - 7800 $\AA$. The observations were carried out on September 9th, 2014 (UT), with a total exposure of a few minutes up to $\sim$ 10 minutes for each star. The final reduced spectra have a signal-to-noise ratio (S/N) of $\sim 100-200$. The motivation of their study was to derive masses using spectroscopic data and check whether this method would be equally reliable as that obtained from seismology. They derived stellar parameters, including surface gravity ($\log g$), metallicity, and effective temperature spectroscopically using Fe lines. Takeda et al. (2016) carried out another observation on July 3rd, 2015 (UT) using the same instrument and reduction procedure as Takeda & Tajitsu (2015), which covered the same wavelength range for 48 new stars in the Kepler field with S/N $\sim$ 100. Thus in this thesis, we have a sample of 90 stars in total (42 stars observed by Takeda & Tajitsu (2015) and 48 new stars observed by Takeda et al. (2016)).

We used asteroseismic results from the Kepler mission to analyze the relation between stellar age and abundance ratios. Mosser et al. (2012) analyzed 218 stars in the Kepler field to obtain the mass and the radius of the stars from the seismic parameters (from now on dubbed $M_{\rm seis}$ and $R_{\rm seis}$). They used Kepler long-cadence data from observations over continuous 690 days, selecting only the stars with the highest signal-to-noise ratio. In addition, they also included short-cadence data from a one-month-long observation (Mosser et al., 2012). They measured global seismic parameters $\Delta\nu$ and $\nu_{\rm max}$, which they used to determine seismic mass $M_{\rm seis}$ through a scaling relation in the form of Equation 4.

Takeda & Tajitsu (2015) and Takeda et al. (2016) re-derived $M_{\rm seis}$ and $R_{\rm seis}$ using their own spectroscopically derived $T_{\rm eff}$, arguing that the $T_{\rm eff}$ provided by the Kepler Input Catalog used by Mosser et al. (2012) is subject to large error. For this purpose, they adopted the scaling relation given by Kallinger et al. (2010), which follows Equation 4, adopting $T_{\rm eff}$ as listed in Table 1 of Takeda & Tajitsu (2015) and Table 1 of Takeda et al. (2016). Furthermore, Takeda et al. (2016) used $M_{\rm seis}$ and the spectroscopic $T_{\rm eff}$ to derive stellar age. They determined the star's position on the HR diagram based on the spectroscopic $T_{\rm eff}$ and created theoretical tracks for each star based on the spectroscopic [Fe/H] and seismic mass $M_{\rm seis}$. First, they determined each star's location on the HR diagram, defined with ($\log T_{\rm eff}$, L). Using the $T_{\rm eff}$ from their spectroscopic observation, they calculated the luminosity from the scaling relation:

$$\log(L/L_\odot) = 4\log(T_{\rm eff,spec}/T_{\rm eff,\odot}) + 2\log(R_{\rm seis}/R_\odot) \tag{12}$$

They assigned a theoretical track for each star using the PARSEC code by Bressan et al. (2012) with super fine grids in the mass of heavy elements Z and stellar initial mass M to check whether the star's location on the HR diagram matches the assigned track. The grid covered $0.06 \leq Z_{\rm grid} \leq 0.0001$ and $1.0M_\odot \leq M \leq 5M_\odot$. The position of the star on the theoretical track is only a function of age since the mass and metallicity are fixed from asteroseismology and spectroscopy, respectively. This gives

age as a result of comparing the actual position of the star with that inferred from the theoretical track. Thus they calculated the age (where age is defined as the time elapsed since the zero-age main sequence (ZAMS) until the present time) by measuring the minimum distance between the nearest track to each data point:

$$d^2(t) = [(10X_\star - 10X_{\rm track}(t))]^2 + [(Y_\star - Y_{\rm track}(t))]^2 \tag{13}$$

the age (t) is naturally derived from this equation, because the proximate point $X_{\rm track}$ and $Y_{\rm track}$ are functions of age only. Since the stars under study here are red giants which have just left the main sequence, their age could be approximated by the time they spent in the main sequence. We adopted the logarithm of the red giants' asteroseismic age from Table 2 of Takeda et al. (2016).

Liu et al. (2019) studied the abundance patterns for the Takeda sample, to determine the differences between red giants and red clump stars by characterizing their chemical properties. They adopted the stellar parameters provided by Takeda & Tajitsu (2015) and Takeda et al. (2016) and determined the metallicity from Fe lines. They determined the abundances of Fe, Na, Al, Mg, Si, Ca, Ti, V, Cr, Ni, Y, Ba, La, and Ce by comparing the observed equivalent widths with theoretical expectations based on the LTE model atmospheres by Kurucz (1993). They also derived the Eu abundance for several stars in their sample.

2.2 Final sample

We select the stars from the sample by visual inspection to verify the presence of adequately strong Th and Eu absorption lines for abundance analysis. This results in a sample of 35 stars with metallicities in the range of $-0.26 \leq [{\rm Fe/H}] \leq 0.37$ (see Table 2), based on the visibility of the weak Th II line at 5989 $\mathring{A}$ and the Eu II line at 6645 $\mathring{A}$. The choice of Eu II line at 6645 $\mathring{A}$ is because this line is well studied and the most reliable compared to other Eu II lines. The Eu II lines at 7301 $\mathring{A}$ and 7217 $\mathring{A}$ are located in regions that are crowded by telluric lines, while the Eu II line at 6437 $\mathring{A}$ is available only for some stars in the sample. Figure 5 shows an example of a star in the analyzed sample. It is shown in the figure that the Th II line is visible to analyze, and the Eu II line is also strongly present. We adopted the individual abundance from Liu et al. (2019), except for Eu since we also aim to derive Eu abundance.

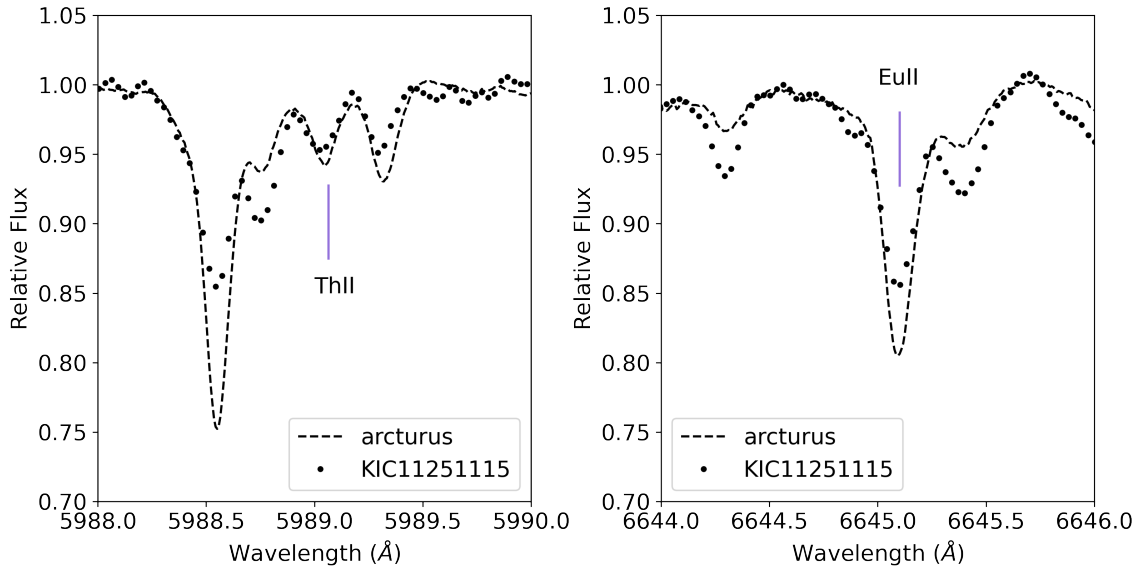

Figure 5: The spectrum of the star KIC11251115, a star in the final sample. The left panel shows the region of the Th II line at 5989 $\AA$ and the right panel shows the Eu II line at 6645 $\AA$. The black dashed line shows the spectrum of Arcturus as the reference, and the dotted line shows the observed spectrum. The positions of the Th and Eu lines are indicated by the short vertical lines.

3 Spectral Analysis

We first determined the shift to move the spectra of our sample into the restframe wavelength. In principle, we could perform this based on any prominent strong line; in this work, we chose a Ti I line in the Th II line region, which is located at 5987.065 $\AA$. The wavelength of the observed line is inferred from visual inspection, which is then used to calculate the shift. An example of a spectrum that has been shifted to the restframe wavelength is shown in Figure 6. It is shown in the figure that the positions of the Ti I and Th II lines in the KIC11251115's spectrum match those in the Arcturus spectrum, which is used as a reference.

We used Turbospectrum spectral synthesis code (Plez, 2012) to create synthetic spectra based on several input parameters, i.e., model atmospheres, individual elemental abundances, metallicity, and line lists. This code first creates the continuum opacity, and then the line profile using line lists. We

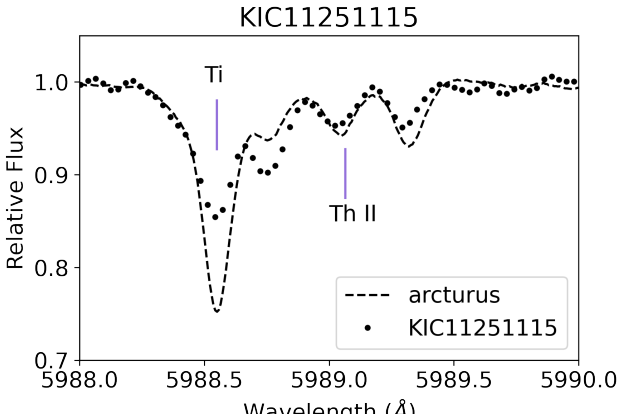

Figure 6: The location of the Ti I line in the region nearby of the Th II line used to calculate the shift for the stars in my sample. The dots show the spectrum of KIC11251115 and the dashed line shows the spectrum of Arcturus used as a reference.

created a model atmosphere for each star from an interpolation of MARCS model atmospheres, which we used as input to the spectral synthesis code. In all cases my sample have the stellar parameters (effective temperature $T_{\rm eff}$, surface gravity $\log g$, and metallicity [Fe/H]) already well determined. We adopted these values to create the model atmospheres. We adopted the default atomic line list of Turbospectrum (Heiter et al., 2021; Magg et al., 2022), which is based on the Gaia-ESO line list, containing the elements, the isotopes, and the number of lines considered for each element. The line list contains, among others, the wavelength, the excitation potential, the oscillator strength ($\log gf$), and the atomic configuration of the upper and lower levels of the transition. We also include molecular line lists from Sneden et al. (2014) and Brooke et al. (2014) containing the CN molecular lines, taking into account the $^{12}C^{14}N$, $^{12}C^{15}N$, and $^{13}C^{14}N$ isotopes in addition to this default atomic line list to accommodate for molecular lines around the region of the Eu II line at 6645 $\AA$. We matched the synthetic spectra with the observed spectrum after smoothing synthetic spectra to take into account the broadening caused by the instrument, macroturbulence, and stellar rotation. We represented all three effects into one broadening parameter, $v_{\rm broad}$. For this purpose, we adopted an initial guess of the broadening parameter of $v_{\rm broad} = 5$ km/s, the typical value for instrumental broadening.

One of the major challenges in abundance analysis is continuum placement. The height of the continuum is by definition known in a synthetic spectrum as set to 1. This is not always so easy in observed spectra. Although the observed spectra are globally continuum-normalized, there are

often some residual fluctuations. We thus need to adjust the continuum locally around the lines. This discrepancy could lead to an offset of 0.2 dex in A_X for Th and 0.1 dex for Eu.

Thus to accurately measure abundances, we correct for this continuum discrepancy such that the continua of the observed and the synthetic spectra match with each other. We calculate the correction factor from the ratio of the observed and synthetic continuum in a narrow region of the spectrum where no obvious absorption lines are present. This factor differs for each spectral region, thus it has to be done separately for the Th and Eu lines. We chose the region between 6646.2-6646.6 $\AA$ to calculate the ratio for the Eu II line at 6645 $\AA$ and 5987.8-5988.2 $\AA$ for the Th II line at 5989 $\AA$. The result of this correction is shown in Figure 7, for an example of a correction to the Th II line region. It is shown that the height of the continuum of the observed spectrum matches better with that of the synthetic spectrum after the correction is made.

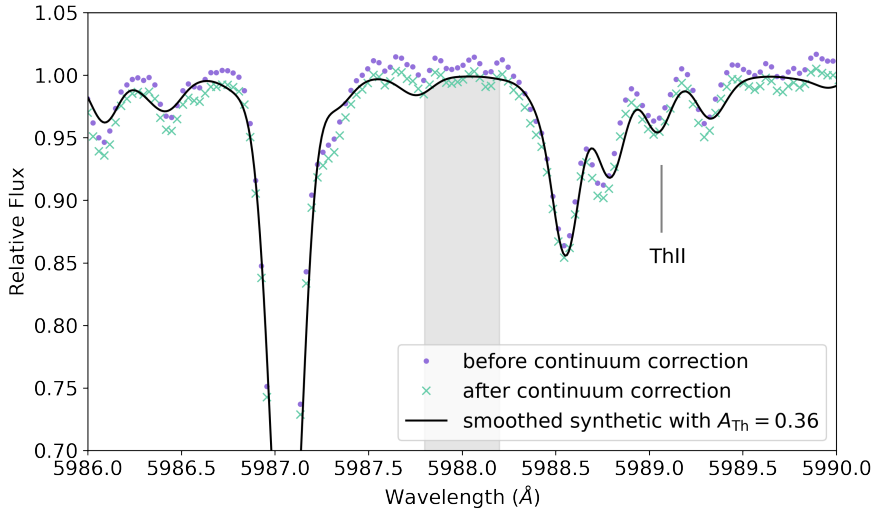

Figure 7: The position of the continuum level before and after adjustment using the synthetic spectrum for the star KIC11251115. The dots show the observed spectrum before correction, and the crosses after the correction. The solid line shows the synthetic spectrum used as a baseline for the continuum correction, assuming the best-fit $A_{\rm Th} = 0.36$. The region selected to calculate the correction scale is indicated by the gray-shaded region, and the position of the Th line is indicated by the short vertical line.

To obtain abundances we analyzed Eu and Th separately, specifying their individual abundances for each analysis. The synthetic spectra are created within regions of 6640-6650 $\AA$ for the Eu II line at 6645 $\AA$ and 5985-5995 $\AA$ for the Th II line at 5989 $\AA$, respectively, with an increment of 0.01 $\AA$. We created a number of synthetic spectra with a change of 0.1 dex in A_X, for a grid of $0.0 - 1.0$ dex. The grid used for Th is $-0.5 - 0.5$, and for some stars with higher Th abundance, a grid of $-0.5 - 1.0$ is required. For the red giant sample, we again adopted the metallicity as given by Takeda & Tajitsu (2015) and Takeda et al. (2016) in creating the synthetic spectra. In addition, we also used other elements' individual abundances determined by Liu et al. (2019) as input in the spectral synthesis code. The individual elemental abundances used in this analysis are Na, Al, Mg, Si, Ca, Ti, V, Cr, Ni, Y, Ba, La, and Ce. For some of the stars, [La/Fe] measurement is not available, thus we assumed the value of $[{\rm La/Fe}] = 0.0$, typical for red giant stars.

To determine the abundances of Th and Eu and also the errors I minimized the χ^2 for the grids to find the synthetic spectrum with a minimal difference from the observed one. We computed the

least squares only for the line of interest. We chose the range of 6644.9-6645.3 $\AA$ for the Eu II line and 5988.95-5989.15 $\AA$ for the Th II line. This choice is based on a visual inspection of the region to ensure that the entire region covering the absorption line under study is included while allowing only minimal contribution from the region outside of it. We determined the broadening parameter with the same minimization manner, adopting the best-fit abundance given above, ranging from $v_{\rm broad} = 5$ km/s to $v_{\rm broad} = 10$ km/s. We iterated this process until convergence is achieved.

After obtaining the best-fit abundance through iteration, to improve precision we created a smaller grid of synthetic spectra with a difference of 0.01 in $A_{\rm X}$ through cubic interpolation, centered at the value of $A_{\rm X}$ determined in the previous step and calculated the least squares for all of them. We repeated the iteration of finding the best-fit $A_{\rm X}$ and the broadening parameter until convergence. As a check, the difference between the interpolated synthetic spectrum and the one generated by Turbospectrum is shown in Figure 8. With the difference in the order of 10^{-16} in normalized flux, thus showing that the interpolated synthetic spectra are good enough to substitute the Turbospectrum generated ones within the finer grid.

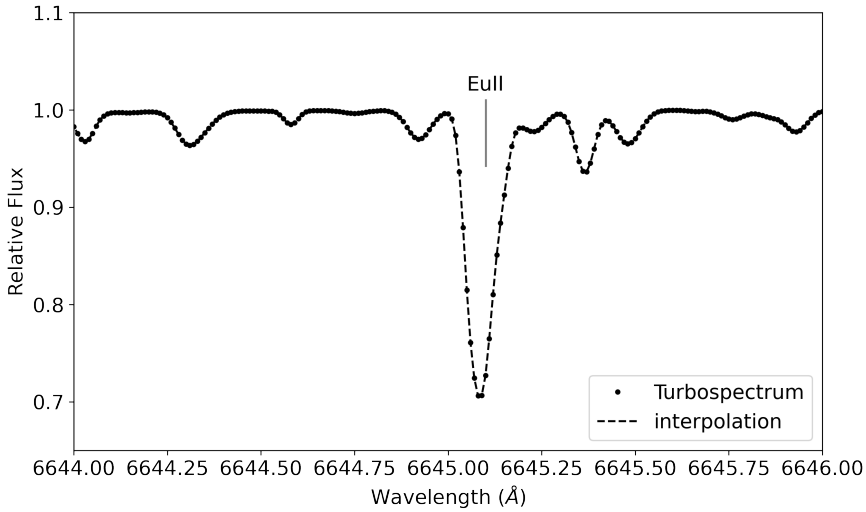

Figure 8: The comparison between the interpolated synthetic spectrum and the one created with Turbospectrum, for the Eu line at 6645 $\AA$ region for the star KIC11251115.

After reaching convergence, we visually check the synthetic spectrum given the best-fit abundance and broadening parameter. The best-fit $A_{\rm X}$ is then converted into the defined notations of [X/H] and [X/Fe], to obtain [Th/Eu] in the end, using Equation 7. We adopted the solar abundances of $A_{\rm Eu} = 0.52$ and $A_{\rm Th} = 0.02$ from Asplund et al. (2009). We also estimate the fitting uncertainty to be ± 0.2 dex based on visual inspection.

4 Results

For my sample of 35 stars, I determined the abundance ratio of [Th/Eu] through spectral synthesis. I determine the Eu and Th abundances as described in the previous section. To ensure that my approach leads to correct results, we first analyzed the Arcturus spectrum before analyzing my sample of red giants in the Kepler field and deriving its abundances. Subsequently, I present the abundance of my sample.

4.1 Arcturus

Arcturus is a well-studied red giant of known abundance and has been studied extensively from extremely high-quality observations. We used this star to confirm Eu abundances using 4 Eu II lines at 6437 $\mathring{A}$, 6645 $\mathring{A}$, 7219 $\mathring{A}$, and 7301 $\mathring{A}$. We also analyzed one Th line at 5989 $\mathring{A}$ and calibrate the line list to analyze my sample of red giant stars.

We used the high-resolution spectrum of Arcturus (Hinkle et al., 2000) covering the wavelength of 3727-9300 $\mathring{A}$. They observed the star using a 0.9-m coude feed telescope and coude spectrograph at Kitt Peak National Observatory. The resolution obtained is on the order of 200000.

For Arcturus, we adopted the metallicity as given by Ramírez & Allende Prieto (2011), $[\mathrm{Fe/H} = -0.5]$. In addition to that, we also specified individual abundances for Si and Nd since these elements contribute to creating absorption lines adjacent to the Th line we are studying. We assumed the relative abundance of $[\mathrm{Si/H}] = -0.19$ as given by Ramírez & Allende Prieto (2011), and $A_{\mathrm{Si},\odot} = 7.51 \pm 0.03$ as given by Asplund et al. (2009), which gives $A_{\mathrm{Si}} = 7.32$. For Nd, we assumed the abundance value for typical disk stars, $[\mathrm{Nd/Fe}] = 0.2$, and $A_{\mathrm{Nd},\odot} = 1.42 \pm 0.04$ as given by Asplund et al. (2009), which gives $A_{\mathrm{Nd}} = 1.12$.

The Eu abundance for Arcturus was determined as described above using 4 lines located at 6437, 6645, 7217, and 7301 $\mathring{A}$ and the default line list provided in the Turbospectrum code including CN molecular lines as described in Section 3. The abundances are shown in Table 1 and the fitting results are shown in Figure 9. It is visible that the synthetic spectra match well with the observed ones for all four Eu II lines we analyzed. The uncertainties quoted in Table 1 are from the uncertainties of the stellar parameters given by (Ramírez & Allende Prieto, 2011).

λ ($\mathring{A}$)	A_{Eu} without CN	A_{Eu} with CN	[Eu/Fe]	$\sigma_{\mathrm{[Eu/Fe]}}$
6437	0.20	0.29	0.27	0.02
6645	0.38	0.36	0.34	0.02
7217	0.31	0.31	0.29	0.02
7301	0.45	0.35	0.33	0.02

Table 1: The Eu abundance in Arcturus, A_{Eu} , for all four Eu II lines we analyzed. We show the values derived before and after we take into account the CN molecules.

The Th abundance was determined as described above using the Th II line at 5989 $\mathring{A}$. As shown in Figure 10, there are several complications in the fit of the Th II. The line is a weak line with several other absorption lines nearby. The most prominent ones are the Si I lines at 5988.791 $\mathring{A}$ and 5988.838 $\mathring{A}$, and a Nd II line at 5989.378 $\mathring{A}$. It is also obvious that the fit of the Th line itself is blended with the much stronger Si I lines, and the position of the Nd II line is not accurate. As Arcturus is a well-studied star, we assumed that the Si abundance is robustly determined. The discrepancy between the observed and synthetic spectra is thus caused by the atomic properties of the transitions, i.e., the

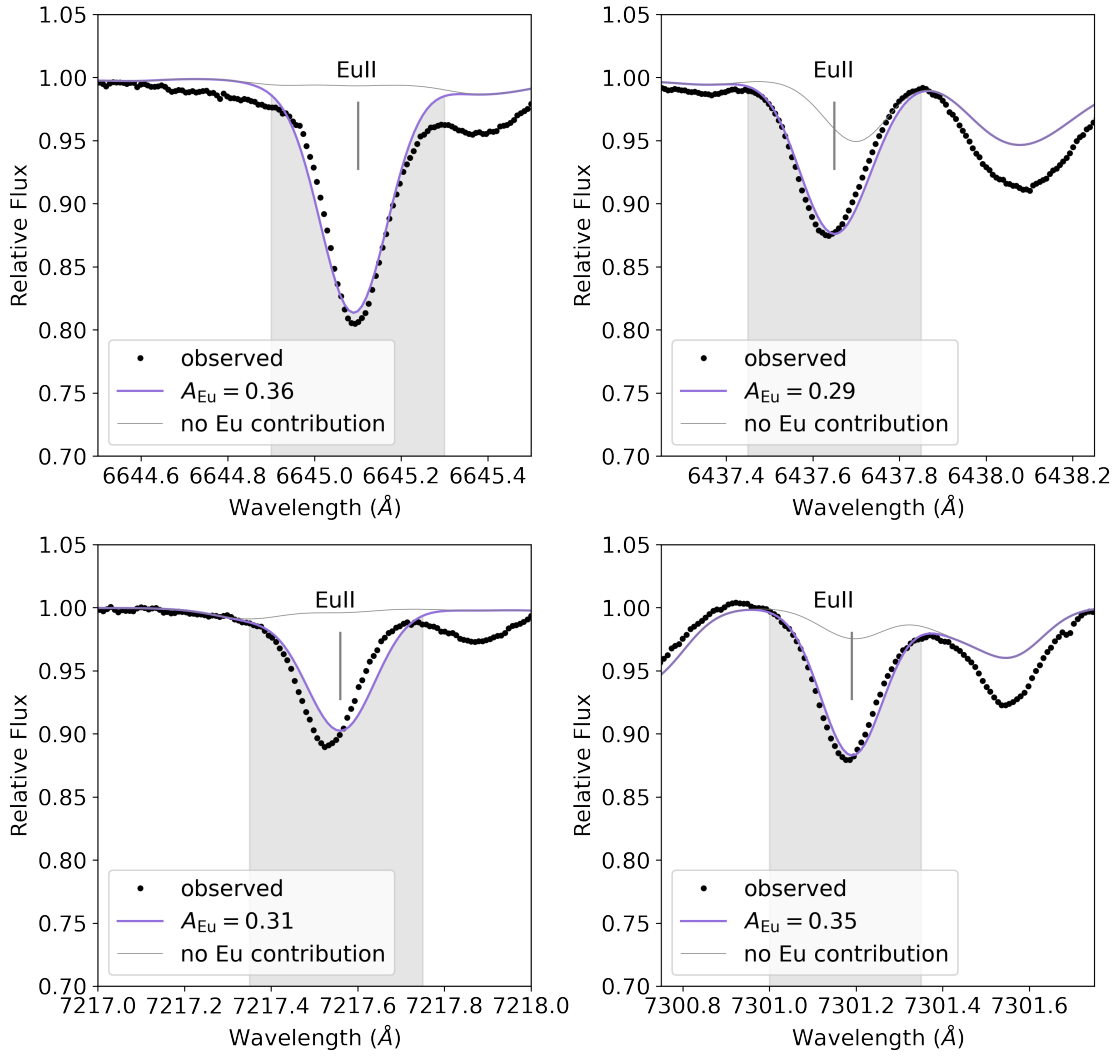

Figure 9: The fitting results of the Eu II lines for Arcturus. Clockwise, from the upper left panel: Eu line at 6645 *Å*, 6437 *Å*, 7301 *Å*, 7217 *Å*, respectively. The best-fit $A_{\rm Eu}$ is indicated in the legend for each panel. The dots show the observed spectrum and the solid line shows the synthetic spectrum after adding the CN molecules. The gray thin line shows a synthetic spectrum where the Eu abundance is assumed to be zero to check for any contamination in the line.

wavelength, excitation potential, and oscillator strength. Thus we decided to adjust these parameters, as we will describe shortly. We adopted a similar approach for the Nd II line.

To correct these problems, we modified the line list in order to improve the fit to the Th II line. We adjusted the oscillator strength of the Si I line at 5988.791 *Å* from $\log gf = -1.653$ to $\log gf = -1.753$ to weaken the line, which is used to fit the Arcturus spectrum. This value is later further adjusted to $\log gf = -2.053$ when applied to fit the spectra of my sample. The oscillator strength of the Si I line

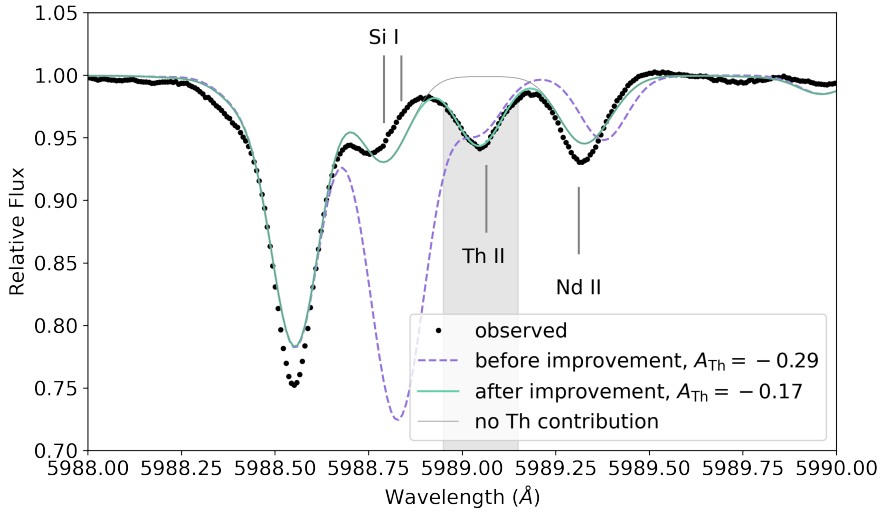

Figure 10: The fitting result of the Th line for Arcturus. The black dotted line shows the observed spectrum, the purple dashed line shows the synthetic spectrum before the line list improvement, and the green solid line shows the synthetic spectrum after the line list improvement. The positions of the Th, Si, and Nd lines are indicated by the short vertical lines. It is visible that the Si and Nd lines are visibly erred before the line list improvement. The gray thin line shows a synthetic spectrum where the Th abundance is assumed to be zero to check for any contamination in the line.

at 5988.838 $\AA$ is changed to $\log gf = -10.851$. We determined these shifts by gradually changing the $\log gf$ values for both lines until the synthetic spectrum matches the observed one. The excitation potential of both lines is 5.964 eV.

Following Aoki et al. (2007), we adjusted the wavelength, excitation potential, and the oscillator strength of the Nd II line from 5989.378 $\AA$ to 5989.312 $\AA$, $\log gf = -1.480$ to $\log gf = -2.05$, and 0.745 to 0.38 eV, respectively. The final result of these improvements is shown in Figure 10. These adjustments resulted in a Th abundance of $A_{\rm Th} = -0.17$ which corresponds to $[{\rm Th/Fe}] = 0.31 \pm 0.03$. For both [Eu/Fe] and [Th/Fe], the quoted uncertainties are from stellar parameters $T_{\rm eff}$, $\log g$, and [Fe/H].

Worley et al. (2009) analyzed the abundance of red giants in 47 Tucanae globular cluster using Arcturus as a standard star. While the study focused on light elements, it also included several heavy elements, including Eu. The Eu abundance they found for Arcturus is $[{\rm Eu/Fe}] = 0.36 \pm 0.04$, which is slightly higher than our average $[{\rm Eu/Fe}] = 0.31$. However, we found that our results are within reasonable agreement with that of Worley et al. (2009), i.e., within errors of both measurements.

Van der Swaelmen et al. (2013) studied the chemical evolution of the Large Magellanic Cloud and compared it to that of the Milky Way using Arcturus as a standard star. They found a value of $[{\rm Eu/Fe}] = 0.41 \pm 0.07$. Although this is slightly higher than our results, we found that our results are in agreement with theirs (within errors) for the [Eu/Fe] derived from the lines at 6645 and 7301 $\AA$. Therefore we are confident that our results are robust.

The study by Worley et al. (2009) did not include Th abundance determination in their analysis. Gopka et al. (1999) performed an abundance analysis of Th in Arcturus, however, we could not find any access to their studies. Holweger (1980) derived Th abundance in Arcturus, Pollux, and Procyon, as the first few stars other than the Sun where Th lines are detectable. They reported a value of $[{\rm Th/H}] = -0.9$, which corresponds to $[{\rm Th/Fe}] = 0.4$, derived from the Th II line at 4019 $\AA$.

This result was derived by employing the oscillator strength from Corliss (1979), which has a total uncertainty of 35% in the f-value. The higher [Th/Fe] they obtained compared to our result might be caused by this uncertainty. They argued that a higher S/N would indeed increase the precision of their abundance determination (Holweger, 1980).

4.2 Main spectroscopic sample

We derived the Eu and Th abundances, along with their solar-scaled values. For all measurements made here of [Eu/Fe] and [Th/Fe] against [Fe/H] are shown in Figure 11. The uncertainties from stellar parameters are estimated to be ± 0.08 in [Eu/Fe], ± 0.05 in [Th/Fe], and ± 0.03 in [Th/Eu] for the most metal-rich star KIC5530598. We expect the uncertainties for other stars in the sample to be of the same order. These uncertainties do not take into account the uncertainty from fitting, which is estimated to be ± 0.2 dex for both A_{Eu} and A_{Th}. The fitting results for all the stars in our sample are shown in Appendix A.

Takeda et al. (2016) provided the ages of the red giants in the logarithmic scale, which we converted into a linear scale. Their results show that there are several stars whose ages are older than the age of the universe, among which one is included in this thesis. In this case, we assumed a maximum age of 14 Gyr in spite of the older asteroseismic age. We present the [Th/Fe], [Eu/Fe], and [Th/Eu] against age in Figure 12. We found that both [Th/Fe] and [Eu/Fe] follow a flat trend against age with some scatter. We will discuss the interpretation of our results in Section 5.

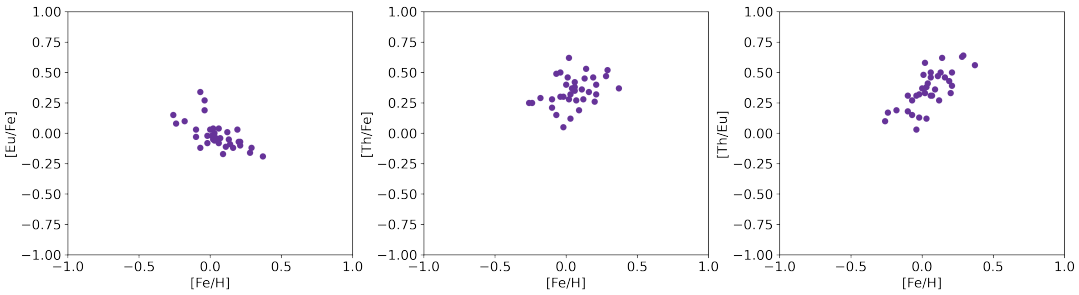

Figure 11: The abundance-metallicity relation of the 35 stars in the sample. From left to right: the [Eu/Fe] trend against metallicity, the [Th/Fe] against metallicity, and [Th/Eu] against metallicity.

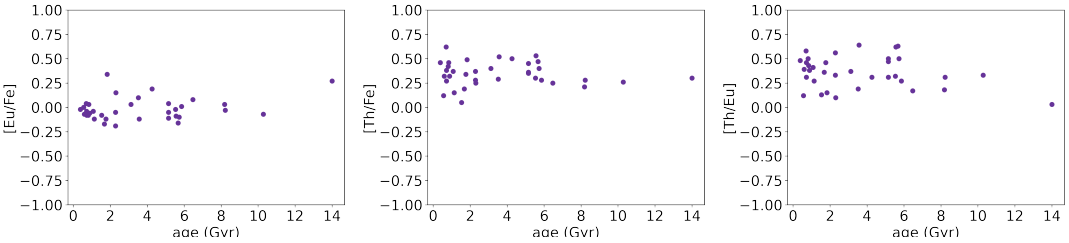

Figure 12: The abundance-age relation of the 35 stars in our sample, shown in large blue data points. From left to right: the [Eu/Fe] trend against age, the [Th/Fe] against age, and [Th/Eu] against age. The small crosses on the right panel show the predicted abundance trend assuming the age given by the asteroseismic data.

KIC ID	$A_{\rm Eu}$	$A_{\rm Th}$	[Fe/H]	[Eu/H]	[Eu/Fe]	[Th/H]	[Th/Fe]	[Th/Eu]	Δ	age (Gyr)
4770846	0.49	0.32	0.02	-0.03	-0.05	0.30	0.28	0.33	0.05	2.29
11352756	0.75	0.28	-0.04	0.23	0.27	0.26	0.30	0.03	0.30	14.00
10709799	0.67	0.48	-0.04	0.15	0.19	0.46	0.50	0.31	0.09	4.27
6276948	0.74	0.67	0.19	0.22	0.03	0.65	0.46	0.43	0.02	0.84
5866737	0.41	0.01	-0.26	-0.11	0.15	-0.01	0.25	0.10	0.05	2.31
2448225	0.56	0.52	0.16	0.04	-0.12	0.50	0.34	0.46	0.04	1.77
2013502	0.42	0.05	-0.02	-0.10	-0.08	0.03	0.05	0.13	0.03	1.54
4243796	0.52	0.49	0.11	0.00	-0.11	0.47	0.36	0.47	0.11	5.15
6117517	0.64	0.77	0.28	0.12	-0.16	0.75	0.47	0.63	0.12	5.68
2573092	0.55	0.42	0.00	0.03	0.03	0.40	0.40	0.37	0.07	3.13
6144777	0.57	0.69	0.14	0.05	-0.09	0.67	0.53	0.62	0.12	5.56
2988638	0.50	0.50	0.06	-0.02	-0.08	0.48	0.42	0.50	0.02	0.81
6579495	0.48	0.3	-0.02	-0.04	-0.02	0.28	0.30	0.32	0.12	5.53
5128171	0.52	0.43	0.04	0.00	-0.04	0.41	0.37	0.41	0.02	1.08
4351319	0.69	0.83	0.29	0.17	-0.12	0.81	0.52	0.64	0.08	3.56
4039306	0.39	0.20	-0.10	-0.13	-0.03	0.18	0.28	0.31	0.18	8.22
2303367	0.62	0.43	0.06	0.10	0.04	0.41	0.35	0.31	0.11	5.15
5806522	0.65	0.42	0.12	0.13	0.01	0.40	0.28	0.27	0.13	5.86
5530598	0.70	0.76	0.37	0.18	-0.19	0.74	0.37	0.56	0.05	2.29
3730953	0.33	0.10	-0.07	-0.19	-0.12	0.08	0.15	0.27	0.02	1.14
9583430	0.66	0.55	0.21	0.14	-0.07	0.53	0.32	0.39	0.01	0.60
5514974	0.45	0.13	-0.10	-0.07	0.03	0.11	0.21	0.18	0.18	8.18
3098045	0.36	0.03	-0.24	-0.16	0.08	0.01	0.25	0.17	0.14	6.47
5088362	0.49	0.37	0.03	-0.03	-0.06	0.35	0.32	0.38	0.02	0.88
5611192	0.58	0.66	0.02	0.06	0.04	0.64	0.62	0.58	0.02	0.70
2424934	0.44	0.13	-0.18	-0.08	0.10	0.11	0.29	0.19	0.08	3.52
4044238	0.65	0.48	0.20	0.13	-0.07	0.46	0.26	0.33	0.22	10.28
5283798	0.44	0.30	0.09	-0.08	-0.17	0.28	0.19	0.36	0.04	1.68
4952717	0.60	0.60	0.13	0.08	-0.05	0.58	0.45	0.50	0.11	5.15
5307747	0.51	0.49	0.01	-0.01	-0.02	0.47	0.46	0.48	0.01	0.38
3455760	0.79	0.44	-0.07	0.27	0.34	0.42	0.49	0.15	0.04	1.83
4902641	0.55	0.17	0.03	0.03	0.00	0.15	0.12	0.12	0.01	0.56
8378462	0.50	0.46	0.06	-0.02	-0.08	0.44	0.38	0.46	0.02	0.72
3217051	0.63	0.63	0.21	0.11	-0.10	0.61	0.40	0.50	0.12	5.73
11251115	0.55	0.36	0.07	0.03	-0.04	0.34	0.27	0.31	0.02	0.72

Table 2: The results for the Kepler red giant sample. Δ denotes the expected abundance ratio difference $\Delta \log N_{\rm Th}/N_{\rm Eu}$. The age on the furthermost right column is adopted from the seismic age derived by Takeda et al. (2016).

5 Discussion

In this section, we discuss the comparison between our results with the previous studies on the Th and Eu abundances. We compare our abundance ratios of [Th/Fe], [Eu/Fe], and [Th/Eu] for our sample with that previous studies of disk stars. We also discuss possible explanations for the discrepancy between our results and the literature.

5.1 New results from this work

We expected that [Th/Eu] vs [Fe/H] should show a flat trend, as Th is exclusively produced by the r-process and Eu is mostly produced by the r-process (only a tiny contribution from s-process (Bisterzo et al., 2014)). This is not what was found in Figure 11. We investigate the abundance behavior as follows, starting from the correlation between abundance and age.

Assuming the seismic ages provided by Takeda et al. (2016), we calculated the expected initial abundance ratio of Th and Eu in logarithmic scale, $\log N_{\rm Th}/N_{\rm Eu}$. We assumed that the Eu does not decay, thus giving a constant abundance through the stellar age. This is because the two most abundant isotopes of Eu, i.e., ^{151}Eu decay with a half-life of 5×10^{18} years, significantly longer than the age of the universe, and ^{153}Eu is a stable isotope. The other Eu isotopes are unstable (decay too fast) and negligible. On the other hand, for Th, we took into account only the most abundant (and stable) isotope, ^{232}Th, with a decay half-life of 1.405×10^{10} years. The other Th isotopes would have been deceased completely, and they have also much smaller contributions and thus are negligible. We calculated the initial abundance based on the following equation:

$$[\mathrm{Th/Eu}]_\star = \left(\log\frac{N_{\rm Th}}{N_{\rm Eu}}\right)_\star - \left(\log\frac{N_{\rm Th}}{N_{\rm Eu}}\right)_\odot \tag{14}$$

$$[\mathrm{Th/Eu}]_\star = \left(\log\frac{N_{\rm Th,0}}{N_{\rm Eu,0}}\right)_\star + \log(\exp(-\lambda_{\rm Th}t_\star)) - \left(\log\frac{N_{\rm Th}}{N_{\rm Eu}}\right)_\odot \tag{15}$$

$$\tag{16}$$

where $t_\star$ denotes the age of the star and $\lambda_{\rm Th} = 0.693/T_{1/2}$ gives the half-lifetime of Th, $T_{1/2}$. We present the trends between the present and initial abundance against age in Figure 13. We present the difference between the current and expected initial abundance in Table 2.

We show the trend between the abundance difference against age in Figure 13. It is visible that the difference is significantly larger for the older stars compared to the younger ones, with the largest difference of $\Delta\log N_{\rm Th}/N_{\rm Eu} = 0.30$. The abundance ratio almost has not decreased yet for the youngest stars.

We examined the age-metallicity relation for the stars in our sample, which we show in the lower left panel in Figure 13. The figure shows no visibly clear trend between the age and metallicity of the stars in our sample. We performed a Pearson's test and found the correlation coefficient to be $r = -0.08$ and the p-value to be $p = 0.67$. This is rather unexpected since older stars should be more metal-poor compared to younger stars, but we found only a rather flat trend with a scatter.

Furthermore, we examined the trends between the abundance ratios, [Eu/H], [Eu/Fe], [Th/H], [Th/Fe], and [Th/Eu] against age, and performed a Pearson's correlation test for each of them. We also show a linear fit for each correlation, using a simple function of $y = ax + b$. We present the results in Figure 14 and the p-values in Table 3. As shown in the figures, the abundance ratios are only weakly correlated with the stellar age, with the slope of the correlation in the order of 10^{-2} and 10^{-3}/Gyr.

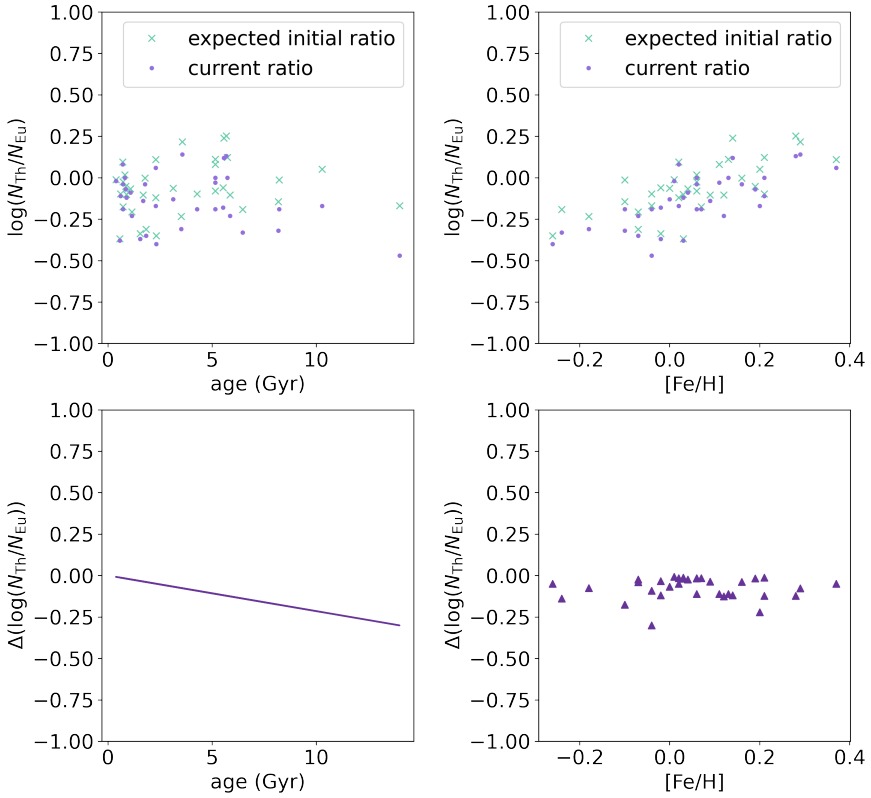

Figure 13: From the upper left panel, clockwise: the current and expected initial ratio of $\log N_{\mathrm{Th}}/N_{\mathrm{Eu}}$ against the stellar age, he current and expected initial ratio of $\log N_{\mathrm{Th}}/N_{\mathrm{Eu}}$ against metallicity, the difference between the current and expected initial value ($\Delta \log N_{\mathrm{Th}}/N_{\mathrm{Eu}}$) against metallicity, and $\Delta \log N_{\mathrm{Th}}/N_{\mathrm{Eu}}$ against age.

It is also clearly visible that for each of the abundance ratio-age relations, the spread is larger for the younger stars compared to the older stars. Furthermore, considering the errors of the slope that are in the same order as the slope itself, i.e., 10^{-2} and 10^{-3}, we can conclude that the slope is consistent with a flat trend without any significant increase or decrease in the abundance ratios against age. The r-values shown in Table 3 indeed show that there are some positive and negative correlations between the abundance ratios and age. However, the r-values are much smaller than 1 with $p > 0.05$ and the correlations cannot be considered statistically significant.

	[Eu/H]	[Eu/Fe]	[Th/H]	[Th/Fe]	[Th/Eu]	[Fe/H]
r-value	0.17	0.25	-0.09	-0.07	-0.24	-0.08
p-value	0.34	0.14	0.61	0.68	0.16	0.67
slope error (/Gyr)	0.006	0.006	0.012	0.007	0.009	0.008

Table 3: The r- and p-values of the abundance ratio vs age trends.

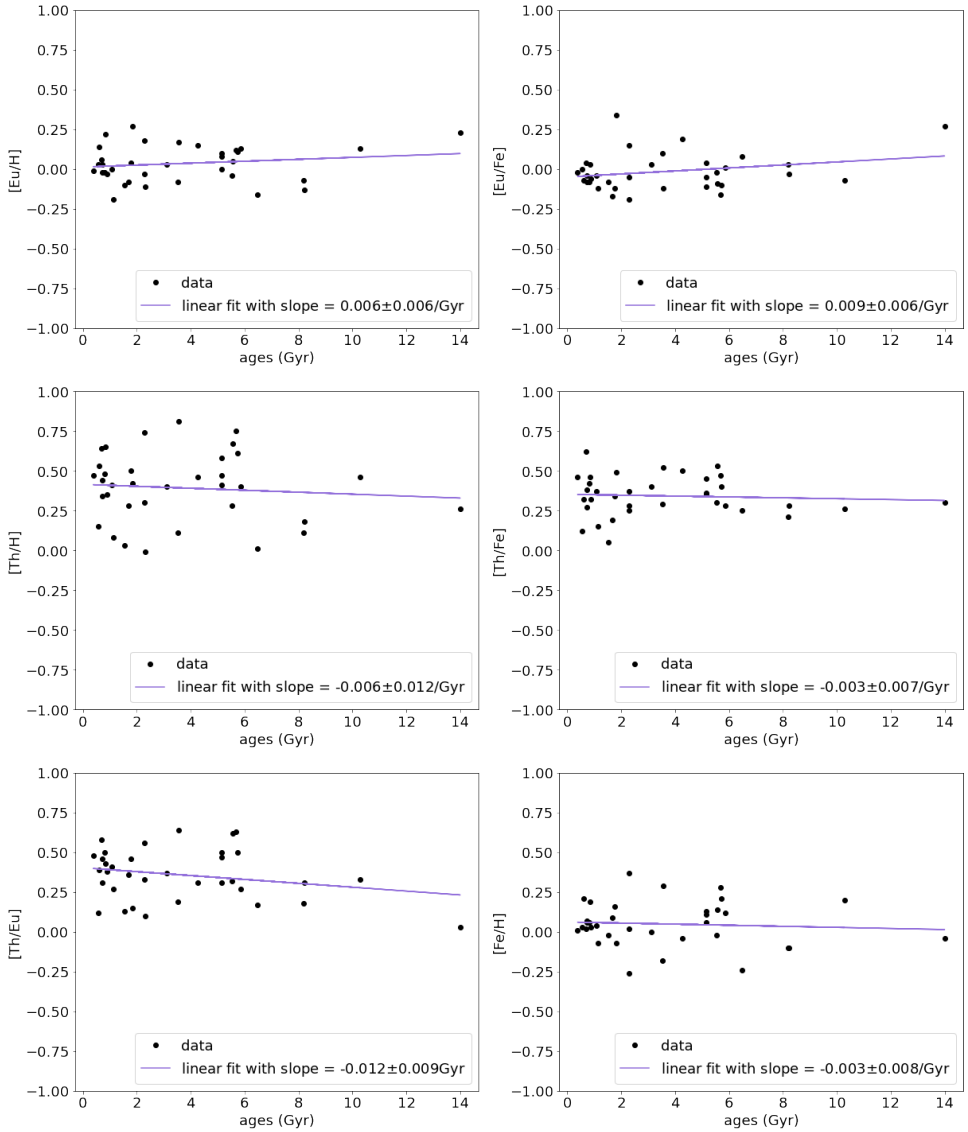

Figure 14: The trends between the abundance ratios against age. Upper left: [Eu/H] and the stellar age, upper right: [Eu/Fe] and age, middle left: [Th/Fe] and age, middle right: [Th/Eu] and age, lower left: [Th/Eu] and age, lower right: [Fe/H] and age. The [Th/Fe] adopted in this result is the value derived after the line list correction.

5.2 Comparison with previous studies

In this section, we proceed to discuss possible sources of discrepancy between our results and expectation from the literature. Mishenina et al. (2022) studied Galactic disk stars to determine the age of the Galactic disk by using a cosmic chronometer. They used the Th II line at 4019 $\AA$ and the Eu II line at 6645$\AA$, which they analyzed previously (Mishenina et al., 2013). The [Eu/Fe] abundance ratio in my sample follows the same trend as found by Mishenina et al. (2022), where the Eu production can be described by the s- and r-processes, with a decreasing trend in higher metallicities due to the production of Fe by SNe Ia. However, we disagree with their derived Th abundance as shown in Figure 15. Our results show significantly and systematically higher [Th/Fe] than literature, especially at solar- and high-metallicities.

There are two obvious explanations for this Th abundance mismatch. The [Th/Fe] for my sample

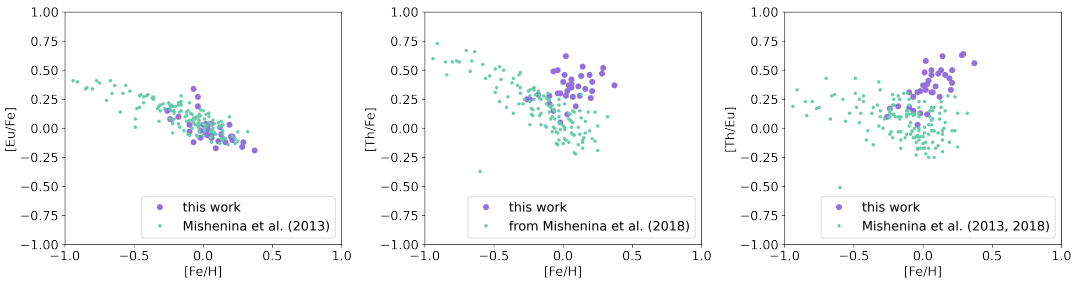

Figure 15: Comparison between the abundance ratio trends we found with that of literature. From top to bottom panel: the trend of [Eu/Fe], [Th/Fe], and [Th/Eu] against metallicity, respectively. The large purple circles are the result obtained in this thesis and the small dots are from Mishenina et al. (2022).

overlap with those of Mishenina et al. (2022) for $-0.25 \leq [\mathrm{Fe/H}] \leq 0.00$, while the stars in my sample with $[\mathrm{Fe/H}] > 0.00$ shows significantly higher [Th/Fe]. This shows that we might have found a similar trend with literature for our low-metallicity stars, but a different trend for the stars at high metallicities. There could also be statistical uncertainties that affect high-metallicity stars more than low-metallicity stars. On the other hand, the stars in our sample seem to follow a rather flat trend, which is also shown by Mishenina et al. (2022)'s sample at $-0.30 \leq [\mathrm{Fe/H}] \leq 0.30$. In this case, our Th abundance is higher than theirs but follows a similar trend. This offset could be a result of the uncertainty of the properties of the Th line we used in this study, that affects all stars in our sample.

Aside from the Th line at 5989 $\AA$ being a very weak line, it is also not widely studied yet. Uncertainties in the atomic properties of the line could lead to uncertainties in abundance determination, e.g., in the wavelength, the excitation potential, and the oscillator strength. There are caveats that cannot be avoided in lab measurements of these quantities. The oscillator strength, $\log gf$ value that we adopted in this study was taken from the lab measurements of Nilsson et al. (2002) and there is no more recent measurement for this line. They reported a total uncertainty of 10% of the gf-value, which translates to uncertainties of $0.04 - 0.05$ dex in $\log gf$, and thus the same amount of uncertainties in A_{X}. In addition to that, the line list we used contains only one Th II line at 5989.045 $\AA$, not taking into account the other transitions of Th II at 5989 $\AA$. There are, in fact, several other lines created by the Th I transitions and also Th II in this region[1]. From Th II, there are other lines located at 5989.200 $\AA$ (excitation potential = 1.89 eV), as well as 5989.893 $\AA$ (excitation potential = 2.62 eV), and 5989.987$\AA$ (excitation potential = 2.60 eV). These lines might be important to consider if they are strong enough to contaminate the line we are considering. There is, however, no information about the measurements of $\log gf$ for these lines.

Previous studies commonly used the Th II line at 4019 $\AA$, and we did not find any previous study on a sample of red giants using the line at 5989 $\AA$. There are, however, several studies using this line for the abundance determination of individual stars. For example, Aoki et al. (2007) studied the Th abundance for a red giant in the Ursa Minor dwarf galaxy, providing the first determination of the Th abundance for an extragalactic object. The 5989 $\AA$ line is much less affected by blending than the line at 4019 $\AA$. The line at 5989 $\AA$ is only slightly contaminated by ^{12}C^{12}C and ^{48}TiO as we show in Figure 17. It is also visible that the effect of contamination is larger for the stars with higher metallicities. The line at 4019 $\AA$, in contrast, is severely blended by other atomic lines, i.e., Fe, Co, Ni, V, Nd, Mn, Ce, as well as CH and CN molecule lines (see Figure 16). It is shown in the figure

[1]NIST Database, accessible on `https://physics.nist.gov/`

that although the line at 4019 $\AA$ is stronger than the one at 5989 $\AA$, it is a result of multiple atomic and molecular contributions. Using 4019 $\AA$ line means that the contributions from each contaminant should be taken into account, especially the contribution from a Co line which is located at almost the same wavelength as the Th line. We believe that our measurement is more reliable due to our choice of a Th line with less contamination.

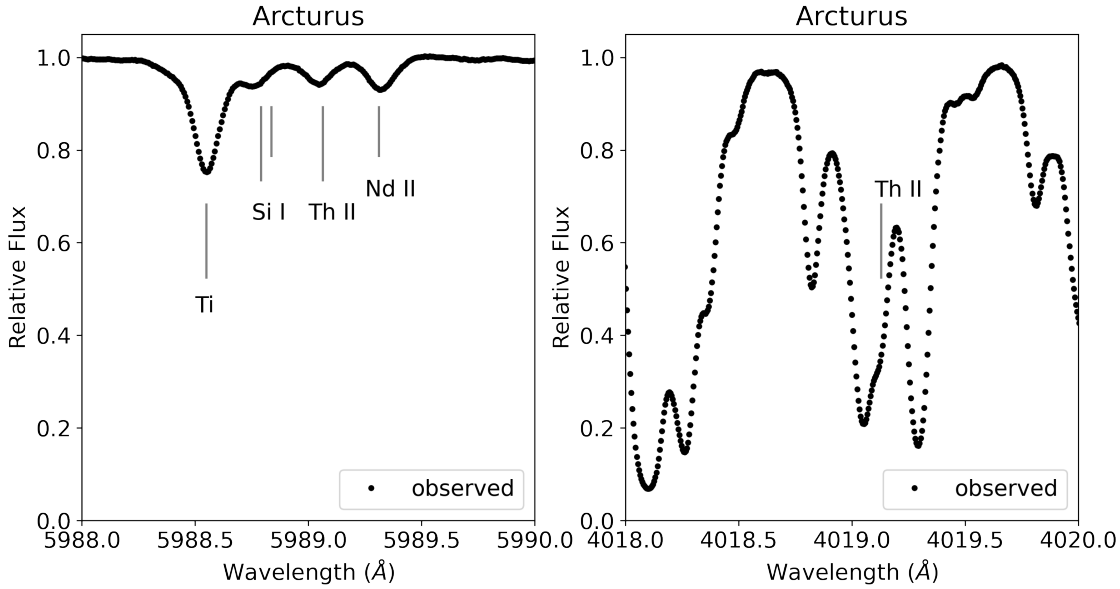

Figure 16: Comparison between the Th II line regions at 5989 $\AA$ (left panel) and 4019 $\AA$ (right panel) in the observed spectrum of Arcturus. The line at 4019 $\AA$ is blended by Fe, Co, Ni, V, Nd, Mn, Ce, CH, and CN within a region of $\sim 0.5\AA$. The contributions are not indicated in the figure due to the crowdedness of the region.

Furthermore, different Th lines might result in different abundances. However, Ivans et al. (2006) studied an r-process-rich star and determined its elemental abundances, including Th, from seven Th lines (3539.59, 3675.57, 3741.18, 4019.12, 4086.52, 4094.75, and 5989.05 $\AA$). The star they studied is HD 221170, an r-process-rich, metal-poor red giant star for which they also provided an age estimate using nucleochronology. They found $[\mathrm{Th/Fe}] = 0.57$ from the Th II line at 5989 $\AA$ and $[\mathrm{Th/Fe}] = 0.6$ from the line at 4019 $\AA$ (Ivans et al., 2006). They also found that their Th/Eu abundance ratio agreed with the scaled solar system r-process abundance and with other r-process-rich stars. Therefore they argued that not only do different Th lines give uniform abundances, but also this abundance determination is quite robust and that this ratio can be used as a chronometer.

Due to the Th abundance discrepancy compared to that of Mishenina et al. (2022), we performed an additional check for contaminations from molecules in the region of the Th line. In addition to the $^{12}C^{14}N$, $^{12}C^{15}N$, and $^{13}C^{14}N$ molecules we have taken into account as described in Section 3, we checked the effect of $^{12}C^{13}C$, $^{12}C^{15}N$, $^{12}C^{14}N$, $^{12}C^{12}C$, ^{12}CH, $^{13}C^{13}C$, $^{13}C^{14}N$, ^{13}CH, ^{14}NH, ^{16}OH, ^{24}MgH, ^{25}MgH, ^{26}MgH, ^{28}SiH, ^{46}TiO, ^{47}TiO, ^{48}TiO, ^{49}TiO, ^{50}TiO, ^{90}ZrO, ^{91}ZrO, ^{92}ZrO, ^{96}ZrO, CaH, FeH, and VO molecules by including the line lists provided by from Gaia-ESO Survey (GES)[2].

First, we chose one star with the highest metallicity to investigate the maximum effect the molecules can have, i.e., KIC5530598 with $[\mathrm{Fe/H}] = 0.37$. We found out that adding $^{12}C^{12}C$ and ^{48}TiO deepens the weak absorption lines, including the Th line. The other molecules do not contribute to any visible contamination. We show this possible contamination in Figure 17 showing the synthetic spectra with

KIC ID	$\Delta_{A_{\rm Th}}$	[Fe/H]
5530598	0.08	0.37
4351319	0.05	0.29
6117517	0.07	0.28
2573092	0.03	0.00
5307747	0.05	0.01
5866737	0.04	-0.26
3098045	0.03	-0.24
2424934	0.03	-0.18

Table 4: The change in the Th abundance, $A_{\rm Th}$, before and after including the molecular line lists from GES in 8 stars for which we performed a further check.

and without the additional molecular lines compared to the observed spectrum.

We performed further checks for 7 other stars with different ranges in metallicities. We picked 3 stars with the lowest metallicities, 2 stars with solar metallicities, and 2 more stars with the highest metallicities. The stars we chose for this purpose are KIC5866737, KIC3098045, KIC2424934, KIC2573092, KIC5307747, KIC6117517, and KIC4351319. We found that the effect is only visually prominent for the most metal-rich stars, though Figure 17 suggests that it might also be important for solar-metallicity stars. We re-derived the $A_{\rm Th}$ for these stars and found slightly lower abundances, as shown in Table 5.2. Although this result might hint at possible contamination, the difference is smaller than 0.1 dex. This is not large enough to explain the different trends of [Th/Fe] between our results and previous investigations. After performing these checks, no plausible explanation has been found for the discrepancy between the Th trend with the expected trend. We conclude that there should be some other cause that has not been examined yet.

We also considered the effects of the model atmospheres we used in creating synthetic spectra. We built our model atmospheres based on MARCS models, which assume 1D LTE conditions. Therefore, any deviations from these assumptions in the stellar photosphere could lead to systematic error in our abundance derivation. Although NLTE effects are not expected to be large for ionized lines such as the Th II line we used. Future detailed NLTE calculation for this line would be of great interest to investigate the possible effects.

As shown in Figure 11, there is scatter both in the [Eu/Fe] and [Th/Fe] against [Fe/H]. The scatter is more prominent in [Th/Fe] compared to [Eu/Fe], which could be caused by measurement uncertainties. This is also reflected by the scatter in the abundance ratio [Th/Eu]. It is also clear that [Eu/Fe] and [Th/Fe] follow distinctly different trends, starting from significantly higher [Th/Fe] than [Eu/Fe] as we have discussed above. The scatter observed in Figure 11 might be caused by observational uncertainties, but it might also hint at different production sites for Eu and Th. We will discuss the possibilities for such a scenario as follows.

It is still debated if there might be more than one r-process in the early Universe contributing to Eu and other heavy r-process elements in metal-poor stars (Mishenina et al., 2022). There might be two sources with different frequencies and timescales contributing to the r-process abundance in metal-poor stars, however, it is also possible that there is only one r-process source contributing with abundance variations (Mishenina et al., 2022). It should also be highlighted that the r-process production in the early universe is different to the present time. A study by Wehmeyer et al. (2015) showed that magnetorotational-driven supernovae and NS mergers are sufficient to explain the r-

process abundance observation as the products of the evolution of massive stars. On the other hand, Eichler et al. (2019) studied Th and Eu production in actinide-boost stars and found that the mixing in the neutron star merger ejecta could lead to variations in [Th/Eu] abundance ratios. Therefore, it is still unclear whether the scatter and variation in our abundance ratios are the result of one or more r-process sources, or merely due to measurement uncertainties.

As we have mentioned previously, we found that there is only a weak correlation between our abundance ratios with age. Spina et al. (2018) studied the correlation between r-process element abundance ratios with age for a sample of solar twin stars (stars with $T_{\rm eff}$, $\log g$, [Fe/H] around that of the Sun) with metallicity as the main selection criterion. They found a tight correlation between [X/Fe] and age, with each element having its own characteristic relation, and that the thin and thick disc stars follow their own distinct trends. For elements with smaller s-process contributions, the slope of the correlation is shallower than those of elements with larger s-process contributions. The tighter correlation between [X/Fe] with age for elements with higher s-process contribution could be interpreted as the result of thin disc AGB star contribution, in which s-process yield is dependent on stellar age. Meanwhile, the thick disc is more enhanced in the r-process elements, i.e., Eu, Gd, and Dy. They argued that the youngest and oldest stars in their sample must have been enriched by different channels of nucleosynthesis, i.e., progenitors of different masses and metallicities. The thick disc stars might have been enriched by mostly metal-poor progenitors, while the thin disc stars are more metal-rich. The new sample here shows an increasing trend for [Eu/Fe], but a decreasing trend for [Th/Fe]. The enhancement in [Eu/Fe] for the stars in our sample might be explained by the enrichment process mentioned above. The information on the thick/thin disc population for our stars might help to disentangle what enrichment processes might have contributed to our abundance determination, though unfortunately, such information is not currently available.

5.3 Future prospects

We found that our [Th/Fe] and [Th/Eu] do not necessarily agree with what might be expected from the literature (Mishenina et al., 2022). There are several possibilities to resolve this issue in future studies. We cover some of the future prospects in this section.

The Takeda sample covered the wavelength region of 5100-7800 $\AA$. It would be useful to obtain the spectra for the sample covering the region of the Th II line at 4019 $\AA$. Although this line is more severely blended by other lines, it is more widely used in Th abundance determination. The availability of this line for this sample would provide a means to check the consistency of the Th abundance measurements from both lines. On the other hand, improvements could also be made to the measurements of the atomic properties of this line. A smaller uncertainty of the $\log gf$ value would improve the accuracy of the abundance derivation. The current uncertainty is 10% of the gf-value for this line, for comparison, the uncertainty of the gf-value for the Th II line at 4019 $\AA$ is 3% ($\log gf = -0.228^{+0.013}_{-0.012}$ (Nilsson et al., 2002)). Another way to check would be to include all the Th transitions at 5989 $\AA$. There are also several other atomic transitions around this line, for example by C, P, Co, Mn, Fe, Mo, Nd, Sm, Yb, and Re, which are included in the line lists. However, we did not assume any individual abundance for these elements, due to the unavailability of a study providing such measurements (except for Fe, which is already taken into account as the input metallicity [Fe/H]). Including these individual abundances might change our results.

[2] https://keeper.mpdl.mpg.de/d/6eaecbf95b88448f98a4/?p=%2Flinelist%2Fmolecules-420-920nm&mode=list

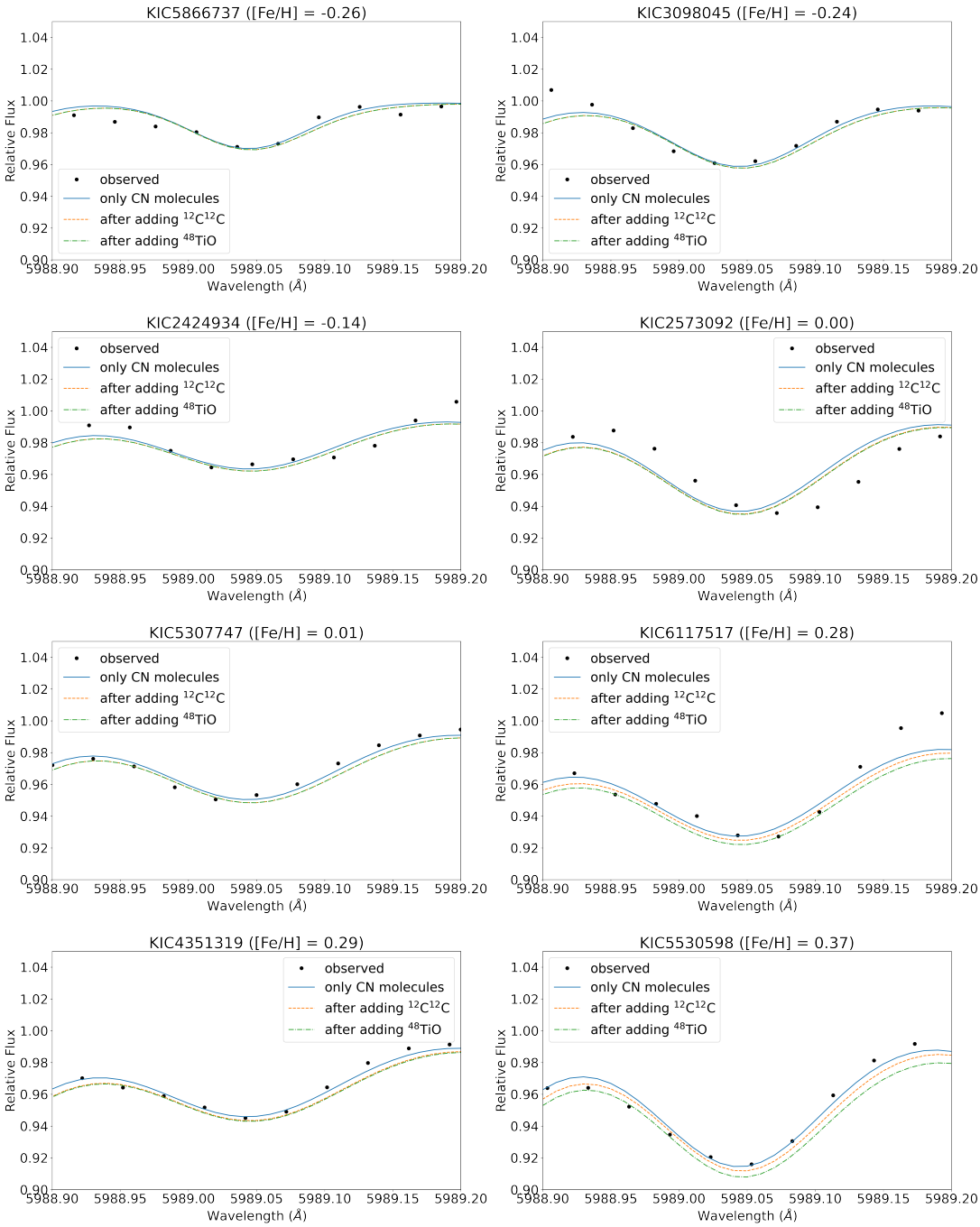

Figure 17: The reasons for the offset between observed and synthetic spectra of the 8 stars for which we checked the effects of additional molecules in the spectra. The star's Kepler ID is indicated on the top of each panel. The blue line shows the synthetic spectrum before adding any new molecules, the orange line shows the spectrum after adding $^{12}C^{12}C$ and the green line after adding ^{48}TiO, successively.

6 Conclusion

Past exoplanet missions such as NASA's Kepler mission have provided an abundance of asteroseismic data for red giants as well as solar-like stars. The wealth of the seismic data has allowed a more reliable stellar mass determination from the observed oscillation frequencies ν_{max} and frequency separation $\Delta\nu$. The seismic masses have been employed to derive more precisely the stellar age. However, stellar age determination using seismic data is rather expensive and complicated to be applied to a large sample of stars, as it requires long and continuous observation times.

In this thesis, I studied the possibility of using the [Th/Eu] chronometer as a method of stellar age determination. I derived the [Th/Eu] abundance for a sample of 35 red giants in the Kepler field, for which the seismic mass and age have been determined. For this purpose, we used the spectral synthesis method, using the Eu II line at 6645 $\AA$, which is widely used and clearly visible in red giant spectra. Furthermore, we explored the use of the Th II line at 5989 $\AA$, which is not widely used.

We found that the [Th/Fe] abundance ratio we derived from this line does not follow the [Eu/Fe] abundance ratio, despite the expectation that Th and Eu are produced together in the r-process nucleosynthesis. The derived [Th/Fe] is higher than the average [Eu/Fe], and while the [Eu/Fe] follows the same trend as previous studies (Mishenina et al., 2022), the [Th/Fe] does not. I also found that the abundance ratios of Th and Eu are only weakly correlated to the stellar age.

I explored several possible explanations for the results that we derived. The [Th/Fe] derived in this study might have suffered from several sources of error. The line itself is a very weak line, rendering its uncertain detection in most stars in the original sample. The weakness of the line does not support accurate abundance measurements. The lab measurements of the line properties (e.g., the central wavelength, the oscillator strength, and the excitation potential) are also subject to uncertainties. I checked the possible contaminations from molecules and found some that might indeed contaminate the line, i.e., $^{12}C^{12}C$ and ^{48}TiO. However, the contamination is negligible in my sample (smaller than 0.1 dex) and so it is not sufficiently large to explain the offset between my results and the literature. On the other hand, this line does not suffer severe blending, in contrast with the case of the Th line at 4019 $\AA$, thus we are confident that our results are not contaminated by other atomic or molecular lines.

We also discussed the possible difference in the production mechanisms and sites for Th and Eu. The scatter and variation in both [Th/Fe] and [Eu/Fe] might be explained by multiple production sites and mechanisms, or one source with abundance variation. The production of r-process elements in NS mergers and CCSNe has been extensively studied. In particular, the mixing in the NS merger ejecta might be responsible for the astrophysical conditions leading to the variation in the Th and Eu abundance produced, resulting in the scatter in the [Th/Eu] abundance ratio. The different trends might also be explained by different enrichment histories for the stars in our sample.

While we found that our Eu abundance is in agreement with the literature, our Th abundance is subject to various uncertainties and is not currently reliable as a chronometer. We believe that future research would benefit the study that we have started in this thesis. For example, performing newer lab measurements of the Th line properties would decrease the uncertainty in the abundance determination using that line. The use of a more complete line list including all atomic and molecular transitions in the region would also help to make sure that there is no additional contamination in the line. Further studies in the r-process production would also benefit not only the understanding of the Th and Eu productions in particular, but also other r-process elements in general.

Bibliography

Aerts, C., Christensen-Dalsgaard, J., & Kurtz, D. W. 2010, Asteroseismology, doi: 10.1007/978-1-4020-5803-5

Aoki, W., Honda, S., Sadakane, K., & Arimoto, N. 2007, PASJ, 59, L15, doi: 10.1093/pasj/59.3.L15

Arcones, A., & Thielemann, F.-K. 2023, A&A Rev., 31, 1, doi: 10.1007/s00159-022-00146-x

Asplund, M., Grevesse, N., Sauval, A. J., & Scott, P. 2009, ARA&A, 47, 481, doi: 10.1146/annurev.astro.46.060407.145222

Bedding, T. R., Huber, D., Stello, D., et al. 2010, ApJ, 713, L176, doi: 10.1088/2041-8205/713/2/L176

Bisterzo, S., Travaglio, C., Gallino, R., Wiescher, M., & Käppeler, F. 2014, ApJ, 787, 10, doi: 10.1088/0004-637X/787/1/10

Bressan, A., Marigo, P., Girardi, L., et al. 2012, MNRAS, 427, 127, doi: 10.1111/j.1365-2966.2012.21948.x

Brooke, J. S. A., Ram, R. S., Western, C. M., et al. 2014, ApJS, 210, 23, doi: 10.1088/0067-0049/210/2/23

Burbidge, E. M., Burbidge, G. R., Fowler, W. A., & Hoyle, F. 1957, Reviews of Modern Physics, 29, 547, doi: 10.1103/RevModPhys.29.547

Butcher, H. R. 1987, Nature, 328, 127, doi: 10.1038/328127a0

Cayrel, R., Spite, M., Spite, F., et al. 2001, in Astronomical Society of the Pacific Conference Series, Vol. 245, Astrophysical Ages and Times Scales, ed. T. von Hippel, C. Simpson, & N. Manset, 244, doi: 10.48550/arXiv.astro-ph/0104448

Corliss, C. H. 1979, MNRAS, 189, 607, doi: 10.1093/mnras/189.3.607

Cowan, J. J., McWilliam, A., Sneden, C., & Burris, D. L. 1997, ApJ, 480, 246, doi: 10.1086/303968

Cowan, J. J., Sneden, C., Lawler, J. E., et al. 2021, Reviews of Modern Physics, 93, 015002, doi: 10.1103/RevModPhys.93.015002

Eichler, M., Sayar, W., Arcones, A., & Rauscher, T. 2019, ApJ, 879, 47, doi: 10.3847/1538-4357/ab24cf

Frebel, A., Christlieb, N., Norris, J. E., et al. 2007, ApJ, 660, L117, doi: 10.1086/518122

Gilliland, R. L., Brown, T. M., Christensen-Dalsgaard, J., et al. 2010, PASP, 122, 131, doi: 10.1086/650399

Gopka, V. F., Yushchenko, A. V., Shavrina, A. V., & Perekhod, A. V. 1999, Kinematika i Fizika Nebesnykh Tel, 15, 447

Goriely, S., & Clerbaux, B. 1999, A&A, 346, 798, doi: 10.48550/arXiv.astro-ph/9904409

Gray, D. F. 1992, The observation and analysis of stellar photospheres., Vol. 20

Hansen, C. J., Montes, F., & Arcones, A. 2014, ApJ, 797, 123, doi: 10.1088/0004-637X/797/2/123

Heiter, U., Lind, K., Bergemann, M., et al. 2021, A&A, 645, A106, doi: 10.1051/0004-6361/201936291

Hekker, S., Kallinger, T., Baudin, F., et al. 2009, A&A, 506, 465, doi: 10.1051/0004-6361/200911858

Hinkle, K., Wallace, L., Valenti, J., & Harmer, D. 2000, Visible and Near Infrared Atlas of the Arcturus Spectrum 3727-9300 A

Holmbeck, E. M., Sprouse, T. M., & Mumpower, M. R. 2023, European Physical Journal A, 59, 28, doi: 10.1140/epja/s10050-023-00927-7

Holweger, H. 1980, The Observatory, 100, 155

Honda, S., Aoki, W., Kajino, T., et al. 2004, ApJ, 607, 474, doi: 10.1086/383406

Ivans, I. I., Simmerer, J., Sneden, C., et al. 2006, ApJ, 645, 613, doi: 10.1086/504069

Jofré, P., Heiter, U., & Soubiran, C. 2019, ARA&A, 57, 571, doi: 10.1146/annurev-astro-091918-104509

Kallinger, T., Weiss, W. W., Barban, C., et al. 2010, A&A, 509, A77, doi: 10.1051/0004-6361/200811437

Koch, D., Borucki, W., Jenkins, J., et al. 2010, in 38th COSPAR Scientific Assembly, Vol. 38, 4

Kurucz, R. 1993, ATLAS9 Stellar Atmosphere Programs and 2 km/s grid. Kurucz CD-ROM No. 13. Cambridge, 13

Lebreton, Y., & Goupil, M. J. 2014, A&A, 569, A21, doi: 10.1051/0004-6361/201423797

Lebreton, Y., Goupil, M. J., & Montalbán, J. 2014, in EAS Publications Series, Vol. 65, EAS Publications Series, ed. Y. Lebreton, D. Valls-Gabaud, & C. Charbonnel, 99–176, doi: 10.1051/eas/1465004

Liu, Y. J., Wang, L., Takeda, Y., Bharat Kumar, Y., & Zhao, G. 2019, MNRAS, 482, 4155, doi: 10.1093/mnras/sty2883

Magg, E., Bergemann, M., Serenelli, A., et al. 2022, A&A, 661, A140, doi: 10.1051/0004-6361/202142971

Mishenina, T., Pignatari, M., Gorbaneva, T., et al. 2022, MNRAS, 516, 3786, doi: 10.1093/mnras/stac2361

Mishenina, T. V., Pignatari, M., Korotin, S. A., et al. 2013, A&A, 552, A128, doi: 10.1051/0004-6361/201220687

Monet, D. G., Jenkins, J. M., Dunham, E. W., et al. 2010, arXiv e-prints, arXiv:1001.0305, doi: 10.48550/arXiv.1001.0305

Mosser, B., Goupil, M. J., Belkacem, K., et al. 2012, A&A, 540, A143, doi: 10.1051/0004-6361/201118519

Nilsson, H., Zhang, Z. G., Lundberg, H., Johansson, S., & Nordström, B. 2002, A&A, 382, 368, doi: 10.1051/0004-6361:20011597

Pagel, B. E. J. 2009, Nucleosynthesis and Chemical Evolution of Galaxies

Plez, B. 2012, Turbospectrum: Code for spectral synthesis, Astrophysics Source Code Library, record ascl:1205.004. http://ascl.net/1205.004

Ramírez, I., & Allende Prieto, C. 2011, ApJ, 743, 135, doi: 10.1088/0004-637X/743/2/135

Roederer, I. U., Kratz, K.-L., Frebel, A., et al. 2009, ApJ, 698, 1963, doi: 10.1088/0004-637X/698/2/1963

Roederer, I. U., Lawler, J. E., Den Hartog, E. A., et al. 2022, ApJS, 260, 27, doi: 10.3847/1538-4365/ac5cbc

Serenelli, A., Weiss, A., Aerts, C., et al. 2021, A&A Rev., 29, 4, doi: 10.1007/s00159-021-00132-9

Silva Aguirre, V., & Serenelli, A. M. 2016, Astronomische Nachrichten, 337, 823, doi: 10.1002/asna.201612379

Sneden, C., Lucatello, S., Ram, R. S., Brooke, J. S. A., & Bernath, P. 2014, ApJS, 214, 26, doi: 10.1088/0067-0049/214/2/26

Spina, L., Meléndez, J., Karakas, A. I., et al. 2018, MNRAS, 474, 2580, doi: 10.1093/mnras/stx2938

Stello, D., Chaplin, W. J., Basu, S., Elsworth, Y., & Bedding, T. R. 2009, MNRAS, 400, L80, doi: 10.1111/j.1745-3933.2009.00767.x

Takeda, Y., & Tajitsu, A. 2015, MNRAS, 450, 397, doi: 10.1093/mnras/stv682

Takeda, Y., Tajitsu, A., Sato, B., et al. 2016, MNRAS, 457, 4454, doi: 10.1093/mnras/stw208

Van der Swaelmen, M., Hill, V., Primas, F., & Cole, A. A. 2013, A&A, 560, A44, doi: 10.1051/0004-6361/201321109

Wanajo, S., Sekiguchi, Y., Nishimura, N., et al. 2018, in Proceedings of the Ito International Research Center Symposium ”Perspectives of the Physics of Nuclear Structure, 012033, doi: 10.7566/JPSCP.23.012033

Wehmeyer, B., Pignatari, M., & Thielemann, F. K. 2015, MNRAS, 452, 1970, doi: 10.1093/mnras/stv1352

Worley, C. C., Cottrell, P. L., Freeman, K. C., & Wylie-de Boer, E. C. 2009, MNRAS, 400, 1039, doi: 10.1111/j.1365-2966.2009.15520.x

Appendix A

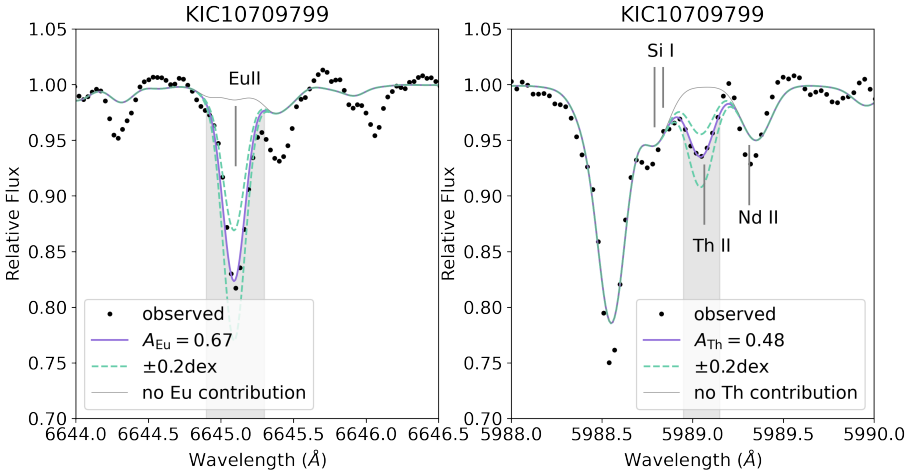
KIC10709799
EuII
Relative Flux
Wavelength (Å)
observed
$A_{Eu} = 0.67$
±0.2dex
no Eu contribution
KIC10709799
Si I
Nd II
Th II
observed
$A_{Th} = 0.48$
±0.2dex
no Th contribution
Wavelength (Å)

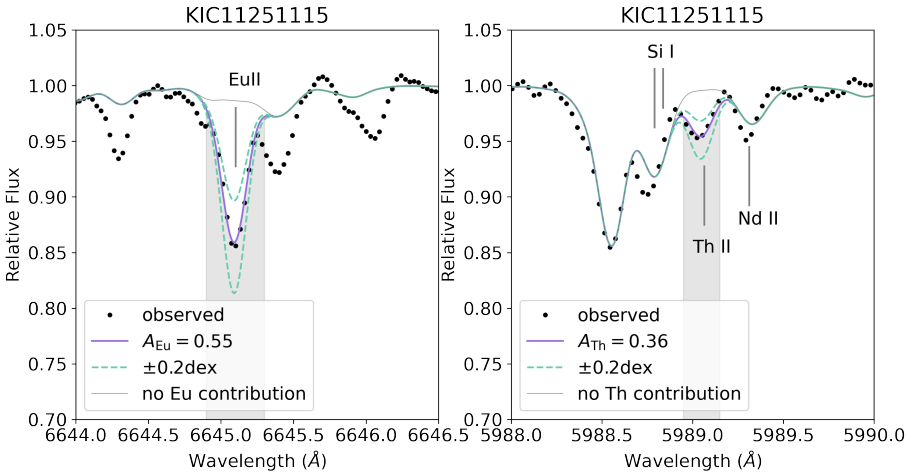
KIC11251115
EuII
Relative Flux
Wavelength (Å)
observed
$A_{Eu} = 0.55$
±0.2dex
no Eu contribution
KIC11251115
Si I
Nd II
Th II
observed
$A_{Th} = 0.36$
±0.2dex
no Th contribution
Wavelength (Å)

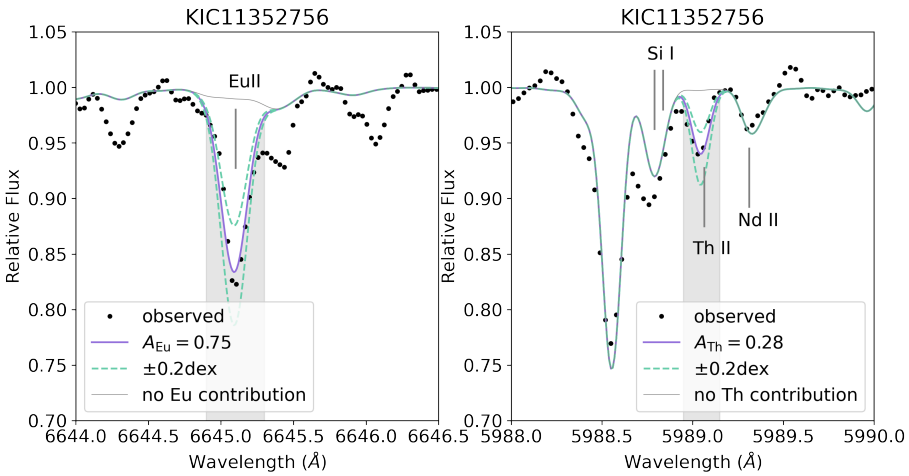
KIC11352756
EuII
Relative Flux
Wavelength (Å)
observed
$A_{Eu} = 0.75$
±0.2dex
no Eu contribution
KIC11352756
Si I
Nd II
Th II
observed
$A_{Th} = 0.28$
±0.2dex
no Th contribution
Wavelength (Å)

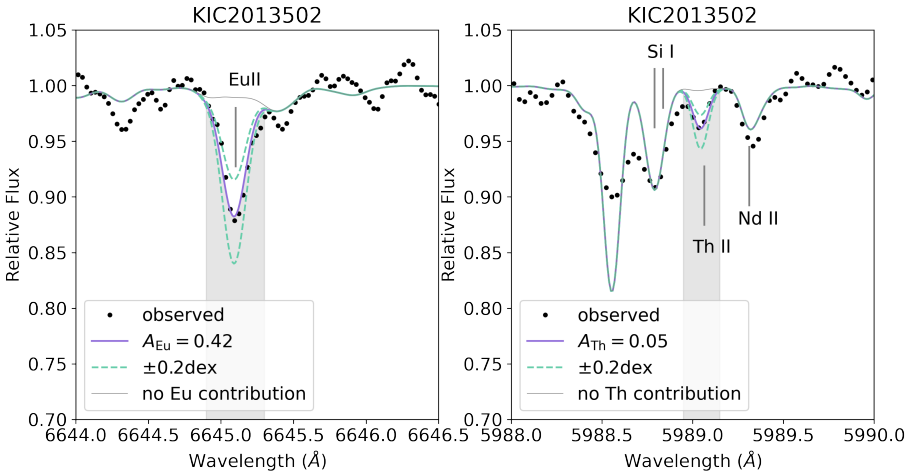
KIC2013502
EuII
Relative Flux
Wavelength (Å)
observed
$A_{Eu} = 0.42$
±0.2dex
no Eu contribution
KIC2013502
Si I
Nd II
Th II
observed
$A_{Th} = 0.05$
±0.2dex
no Th contribution

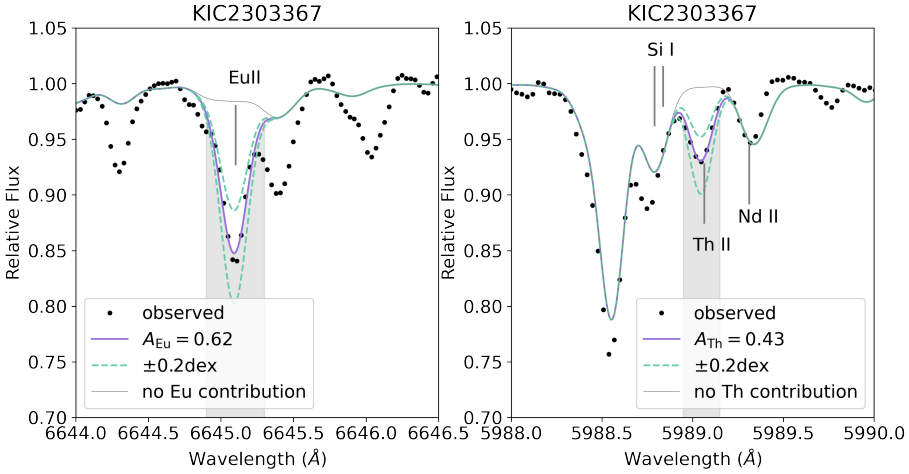
KIC2303367
EuII
Relative Flux
Wavelength (Å)
observed
$A_{Eu} = 0.62$
±0.2dex
no Eu contribution
KIC2303367
Si I
Nd II
Th II
observed
$A_{Th} = 0.43$
±0.2dex
no Th contribution

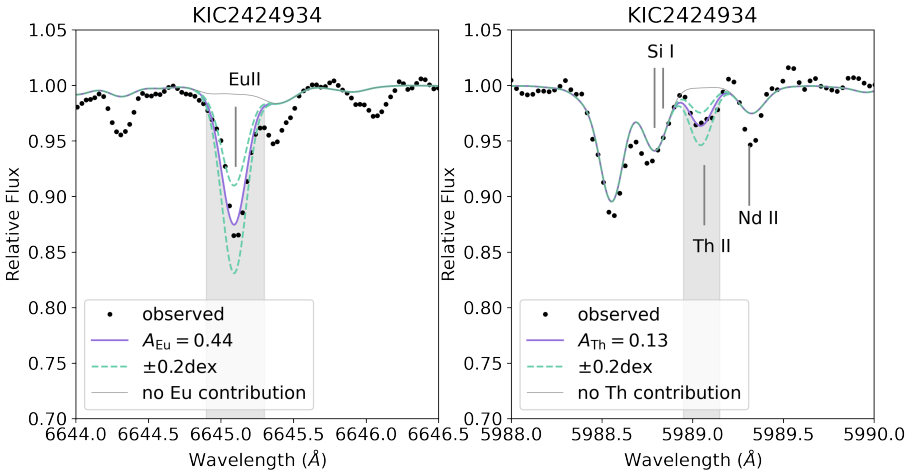
KIC2424934
EuII
Relative Flux
Wavelength (Å)
observed
$A_{Eu} = 0.44$
±0.2dex
no Eu contribution
KIC2424934
Si I
Nd II
Th II
observed
$A_{Th} = 0.13$
±0.2dex
no Th contribution

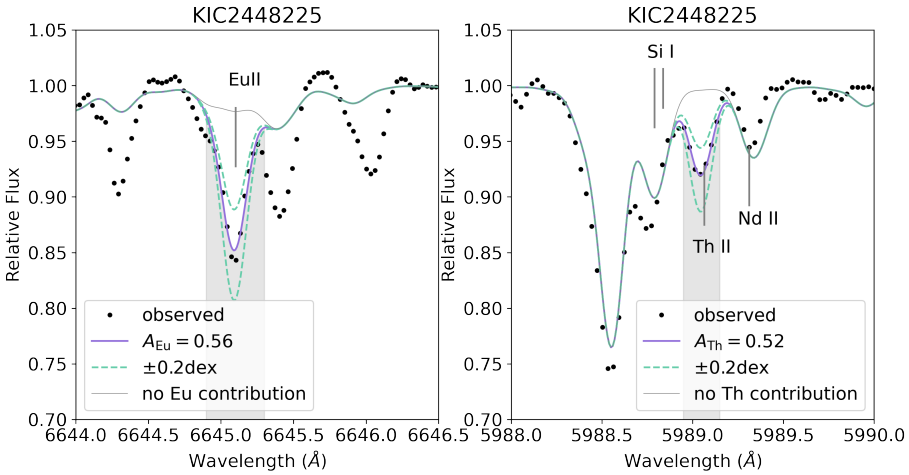
KIC2448225
EuII
Relative Flux
Wavelength (Å)
observed
$A_{Eu} = 0.56$
±0.2dex
no Eu contribution
KIC2448225
Si I
Nd II
Th II
observed
$A_{Th} = 0.52$
±0.2dex
no Th contribution

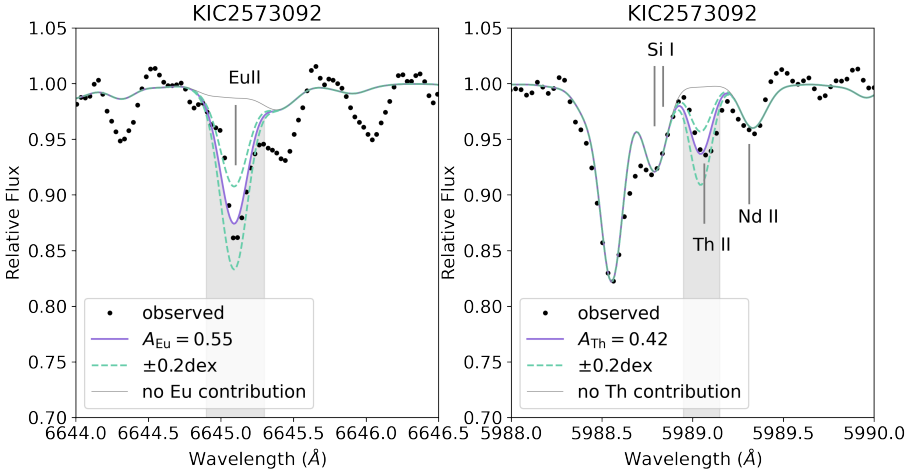
KIC2573092
EuII
Relative Flux
Wavelength (Å)
observed
$A_{Eu} = 0.55$
±0.2dex
no Eu contribution
KIC2573092
Si I
Nd II
Th II
observed
$A_{Th} = 0.42$
±0.2dex
no Th contribution

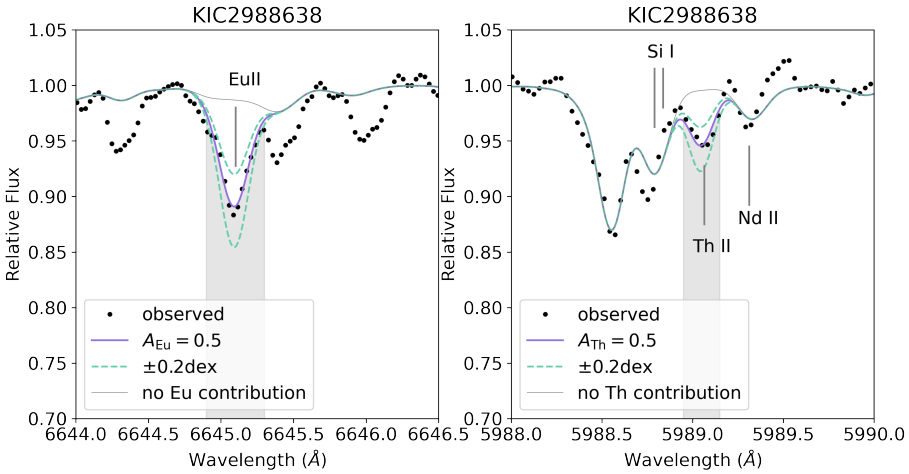
KIC2988638
EuII
Relative Flux
Wavelength (Å)
observed
$A_{Eu} = 0.5$
±0.2dex
no Eu contribution
KIC2988638
Si I
Nd II
Th II
observed
$A_{Th} = 0.5$
±0.2dex
no Th contribution

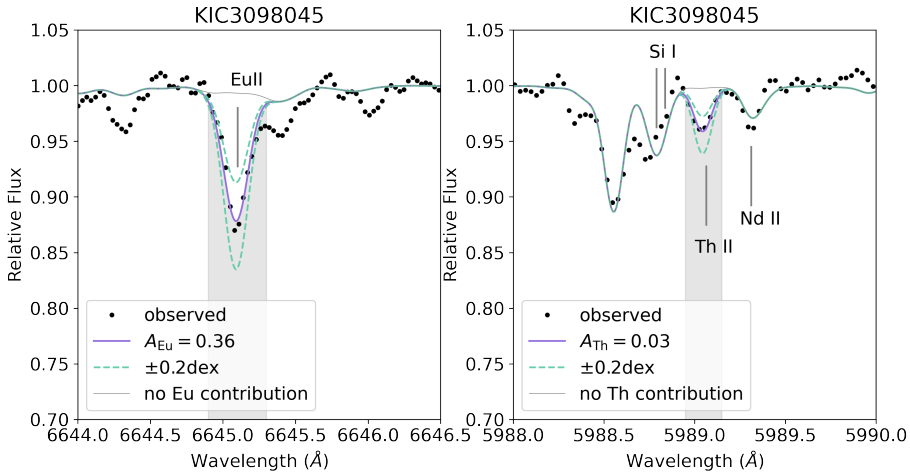
KIC3098045
EuII
Relative Flux
Wavelength (Å)
observed
$A_{Eu} = 0.36$
±0.2dex
no Eu contribution
KIC3098045
Si I
Nd II
Th II
Relative Flux
Wavelength (Å)
observed
$A_{Th} = 0.03$
±0.2dex
no Th contribution

Figure A.1

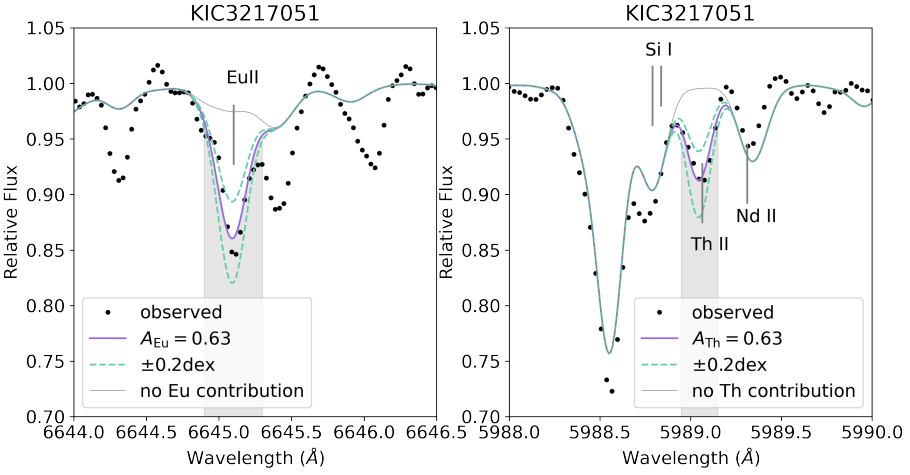
KIC3217051
EuII
Relative Flux
Wavelength (Å)
observed
$A_{Eu} = 0.63$
±0.2dex
no Eu contribution
KIC3217051
Si I
Nd II
Th II
Relative Flux
Wavelength (Å)
observed
$A_{Th} = 0.63$
±0.2dex
no Th contribution

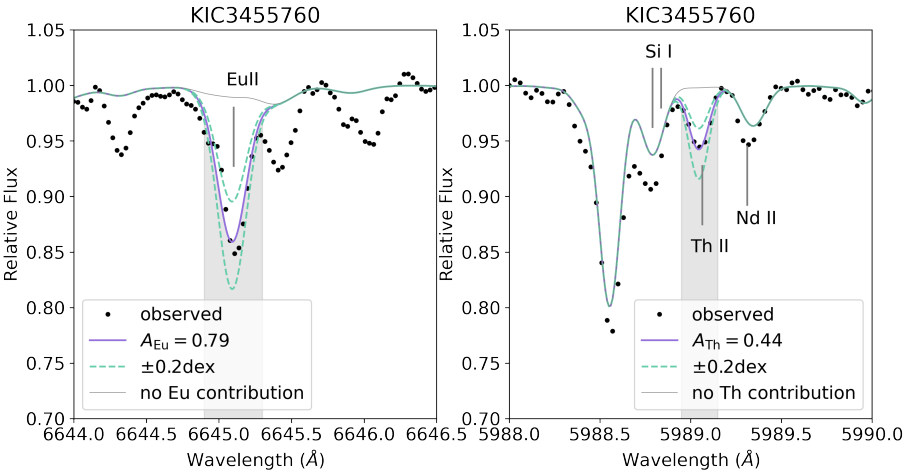
KIC3455760
EuII
Relative Flux
Wavelength (Å)
observed
$A_{Eu} = 0.79$
±0.2dex
no Eu contribution
KIC3455760
Si I
Nd II
Th II
Relative Flux
Wavelength (Å)
observed
$A_{Th} = 0.44$
±0.2dex
no Th contribution

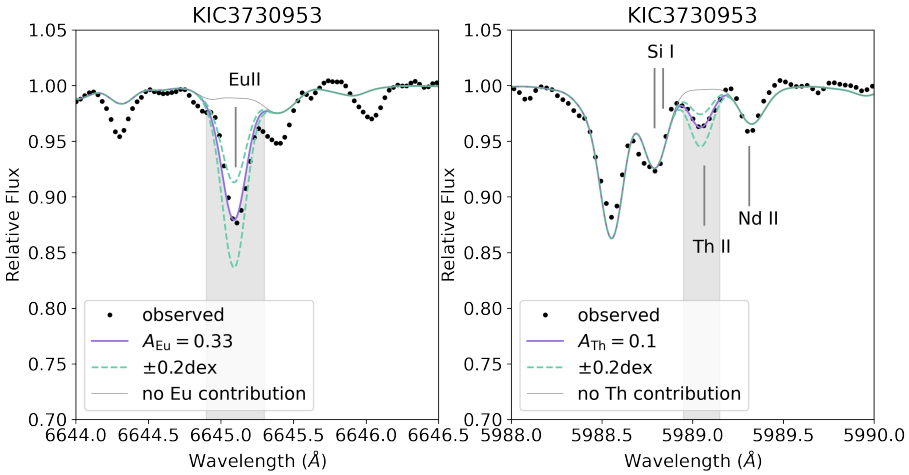
KIC3730953
EuII
Relative Flux
Wavelength (Å)
observed
$A_{Eu} = 0.33$
±0.2dex
no Eu contribution
KIC3730953
Si I
Nd II
Th II
observed
$A_{Th} = 0.1$
±0.2dex
no Th contribution

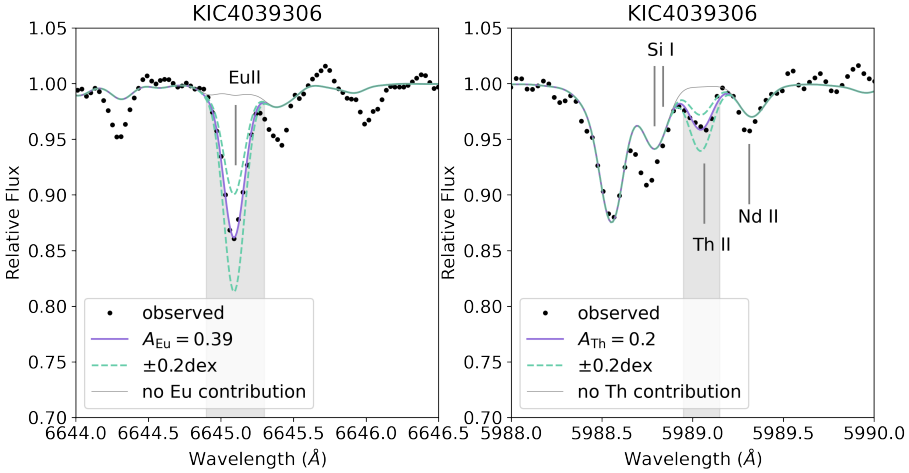
KIC4039306
EuII
Relative Flux
Wavelength (Å)
observed
$A_{Eu} = 0.39$
±0.2dex
no Eu contribution
KIC4039306
Si I
Nd II
Th II
observed
$A_{Th} = 0.2$
±0.2dex
no Th contribution

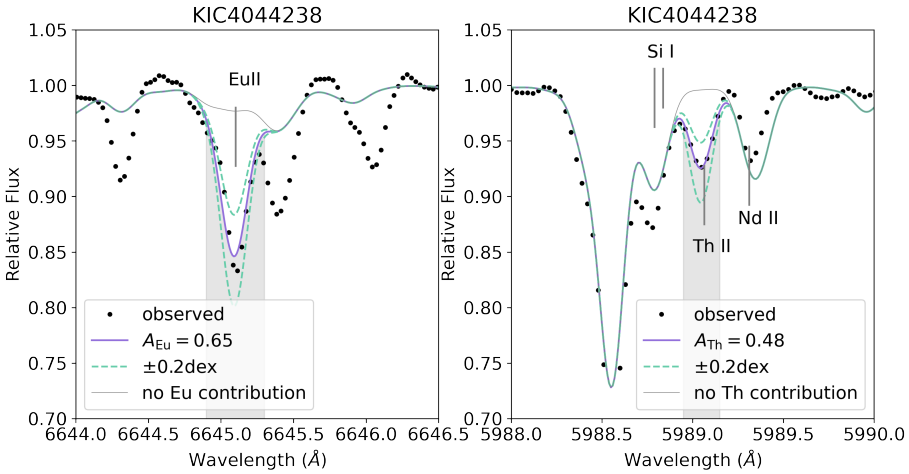
KIC4044238
EuII
Relative Flux
Wavelength (Å)
observed
$A_{Eu} = 0.65$
±0.2dex
no Eu contribution
KIC4044238
Si I
Nd II
Th II
observed
$A_{Th} = 0.48$
±0.2dex
no Th contribution

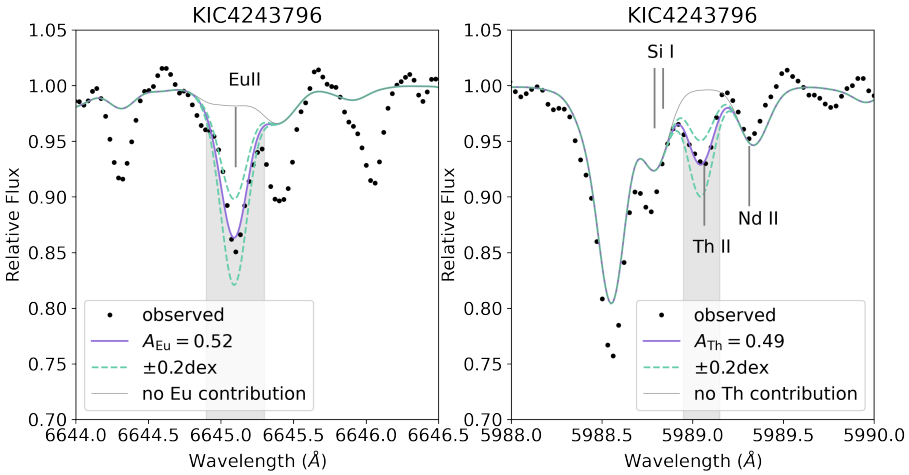
KIC4243796
EuII
Relative Flux
Wavelength (Å)
observed
$A_{Eu} = 0.52$
±0.2dex
no Eu contribution
KIC4243796
Si I
Nd II
Th II
observed
$A_{Th} = 0.49$
±0.2dex
no Th contribution

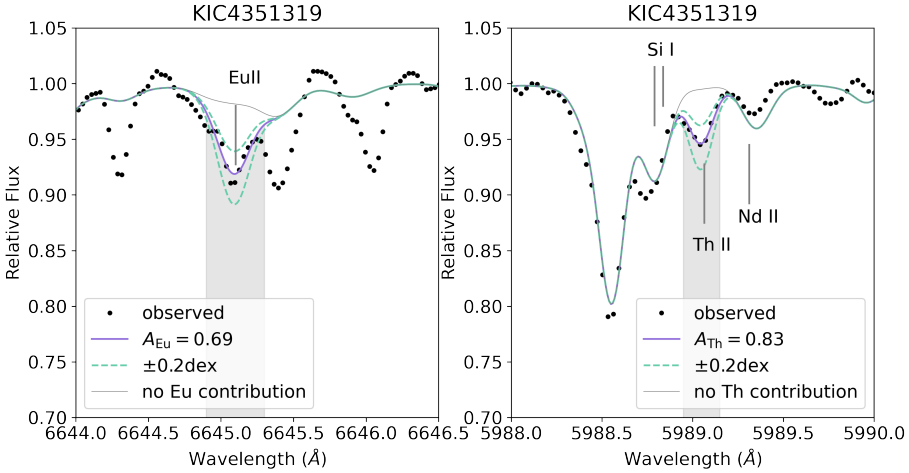
KIC4351319
EuII
Relative Flux
Wavelength (Å)
observed
$A_{Eu} = 0.69$
±0.2dex
no Eu contribution
KIC4351319
Si I
Nd II
Th II
observed
$A_{Th} = 0.83$
±0.2dex
no Th contribution

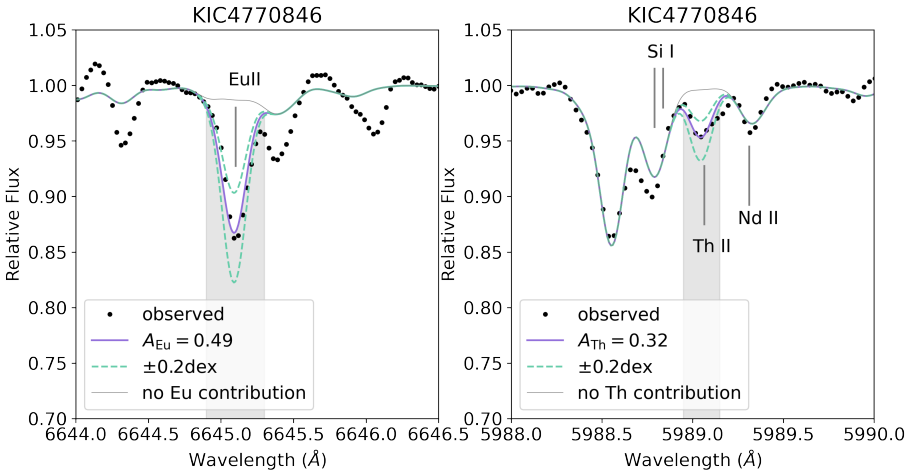
KIC4770846
EuII
Relative Flux
Wavelength (Å)
observed
$A_{Eu} = 0.49$
±0.2dex
no Eu contribution
KIC4770846
Si I
Nd II
Th II
observed
$A_{Th} = 0.32$
±0.2dex
no Th contribution

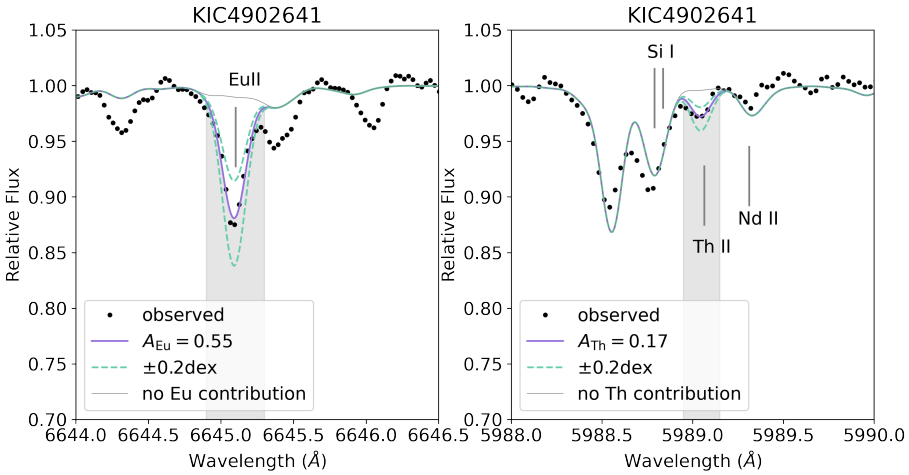
KIC4902641
EuII
Relative Flux
Wavelength (Å)
observed
$A_{Eu} = 0.55$
±0.2dex
no Eu contribution
KIC4902641
Si I
Nd II
Th II
$A_{Th} = 0.17$
no Th contribution

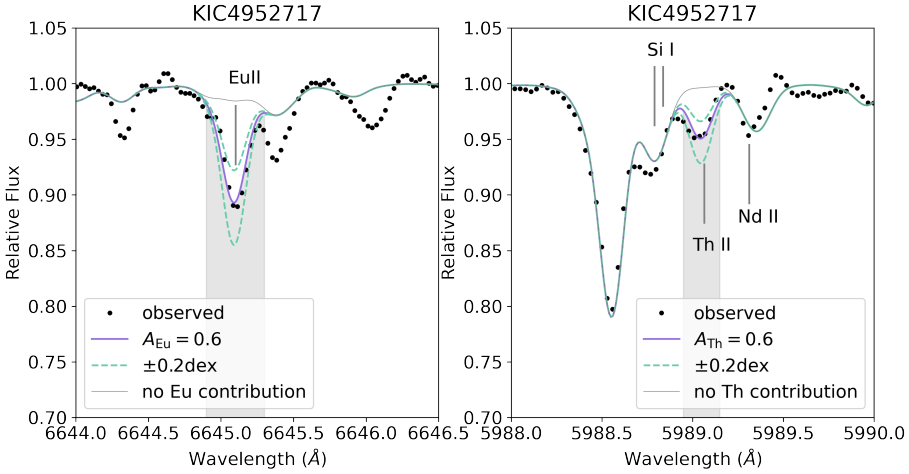
KIC4952717
EuII
Relative Flux
Wavelength (Å)
observed
$A_{Eu} = 0.6$
±0.2dex
no Eu contribution
KIC4952717
Si I
Nd II
Th II
$A_{Th} = 0.6$
no Th contribution

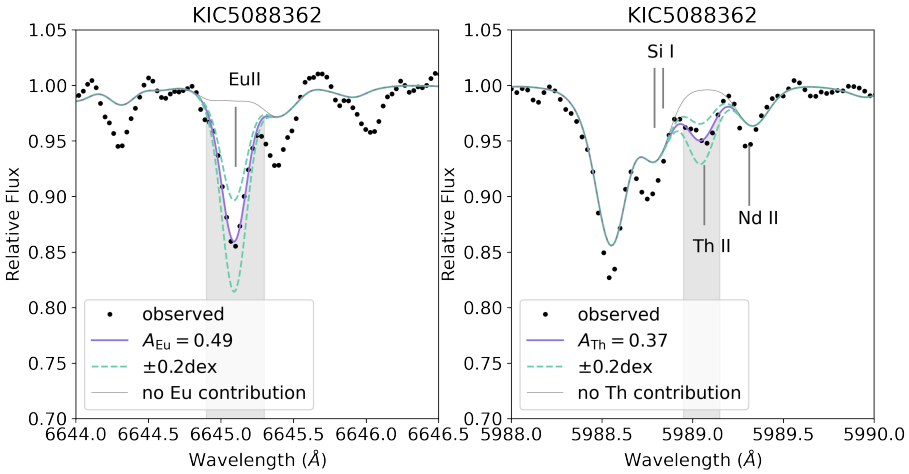
KIC5088362
EuII
Relative Flux
Wavelength (Å)
observed
$A_{Eu} = 0.49$
±0.2dex
no Eu contribution
KIC5088362
Si I
Nd II
Th II
$A_{Th} = 0.37$
no Th contribution

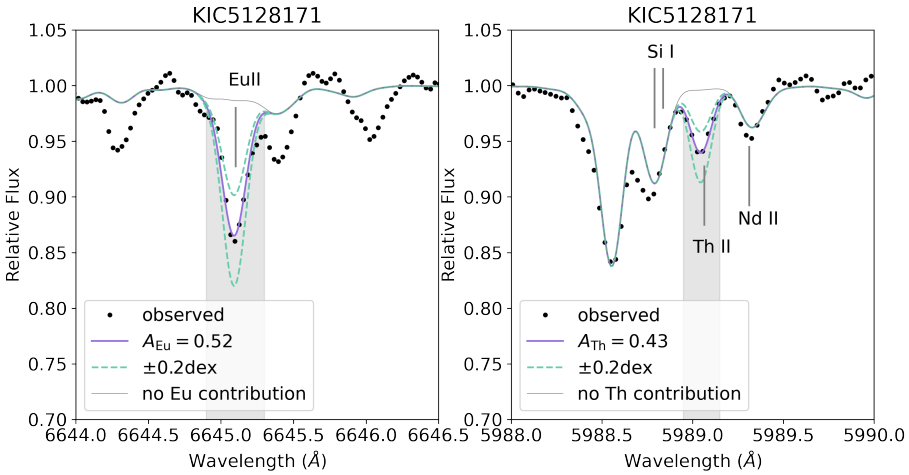
KIC5128171
EuII
Relative Flux
Wavelength (Å)
observed
$A_{Eu} = 0.52$
±0.2dex
no Eu contribution
KIC5128171
Si I
Nd II
Th II
observed
$A_{Th} = 0.43$
±0.2dex
no Th contribution

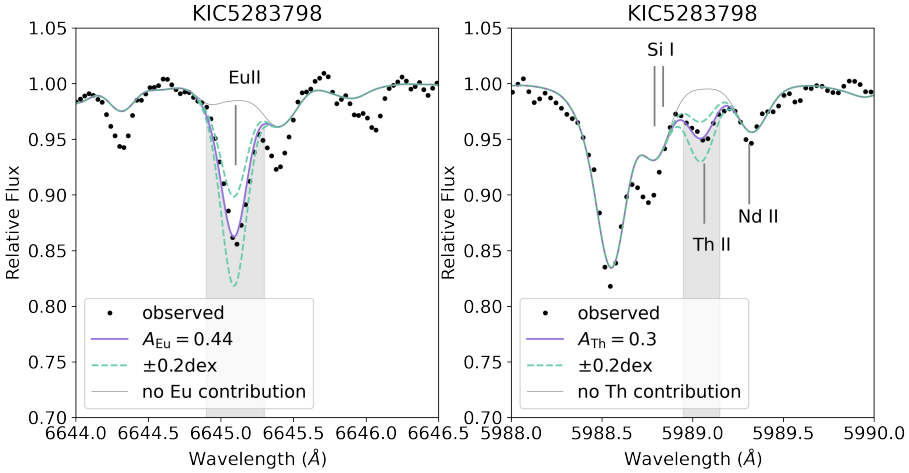
KIC5283798
EuII
Relative Flux
Wavelength (Å)
observed
$A_{Eu} = 0.44$
±0.2dex
no Eu contribution
KIC5283798
Si I
Nd II
Th II
observed
$A_{Th} = 0.3$
±0.2dex
no Th contribution

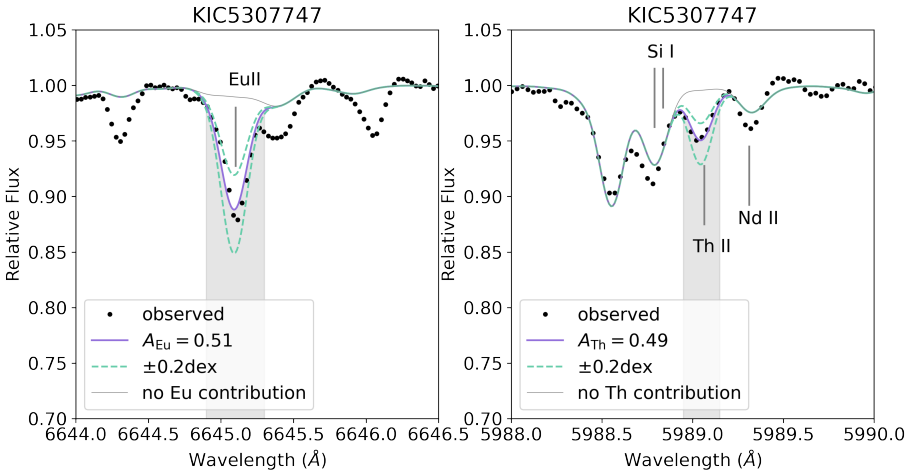
KIC5307747
EuII
Relative Flux
Wavelength (Å)
observed
$A_{Eu} = 0.51$
±0.2dex
no Eu contribution
KIC5307747
Si I
Nd II
Th II
observed
$A_{Th} = 0.49$
±0.2dex
no Th contribution

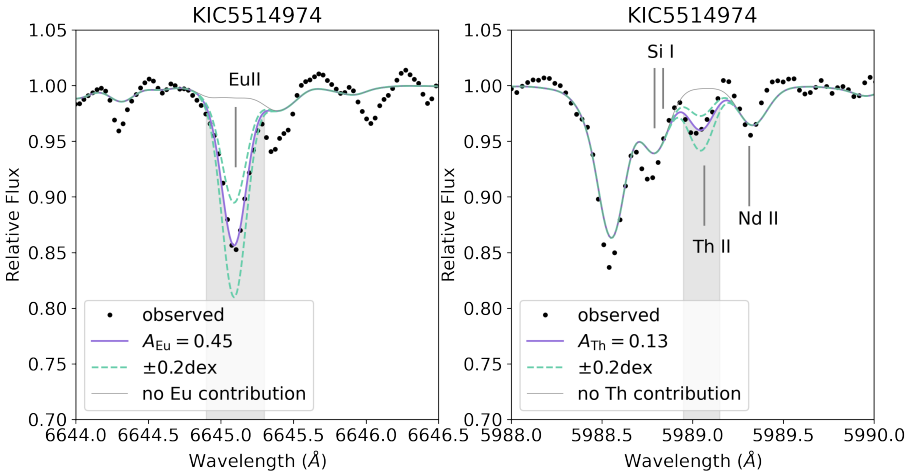
KIC5514974
EuII
observed
$A_{Eu} = 0.45$
±0.2dex
no Eu contribution
Relative Flux
Wavelength (Å)
KIC5514974
Si I
Nd II
Th II
observed
$A_{Th} = 0.13$
±0.2dex
no Th contribution
Relative Flux
Wavelength (Å)

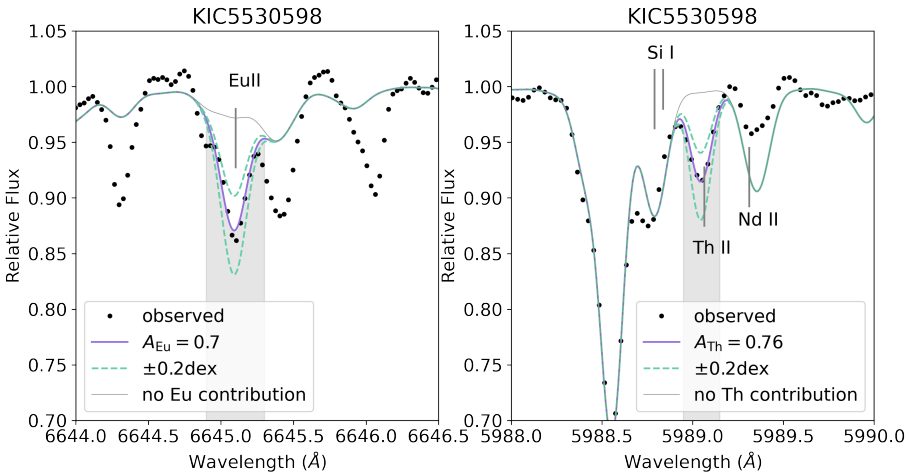
KIC5530598
EuII
observed
$A_{Eu} = 0.7$
±0.2dex
no Eu contribution
Relative Flux
Wavelength (Å)
KIC5530598
Si I
Nd II
Th II
observed
$A_{Th} = 0.76$
±0.2dex
no Th contribution
Relative Flux
Wavelength (Å)

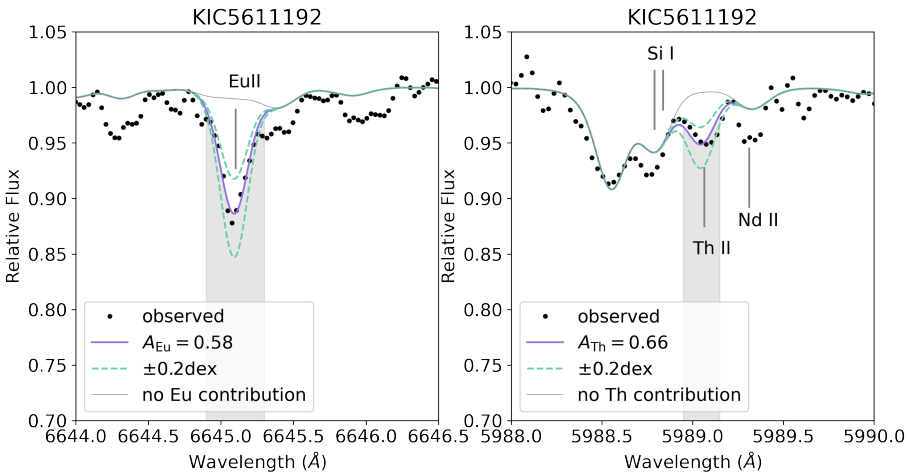
KIC5611192
EuII
observed
$A_{Eu} = 0.58$
±0.2dex
no Eu contribution
Relative Flux
Wavelength (Å)
KIC5611192
Si I
Nd II
Th II
observed
$A_{Th} = 0.66$
±0.2dex
no Th contribution
Relative Flux
Wavelength (Å)

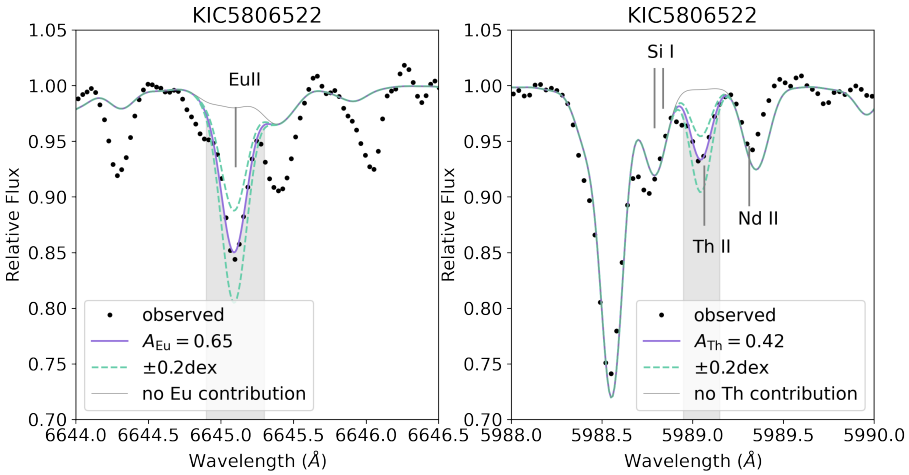
KIC5806522
EuII
Relative Flux
Wavelength (Å)
observed
$A_{Eu} = 0.65$
±0.2dex
no Eu contribution
KIC5806522
Si I
Nd II
Th II
observed
$A_{Th} = 0.42$
±0.2dex
no Th contribution

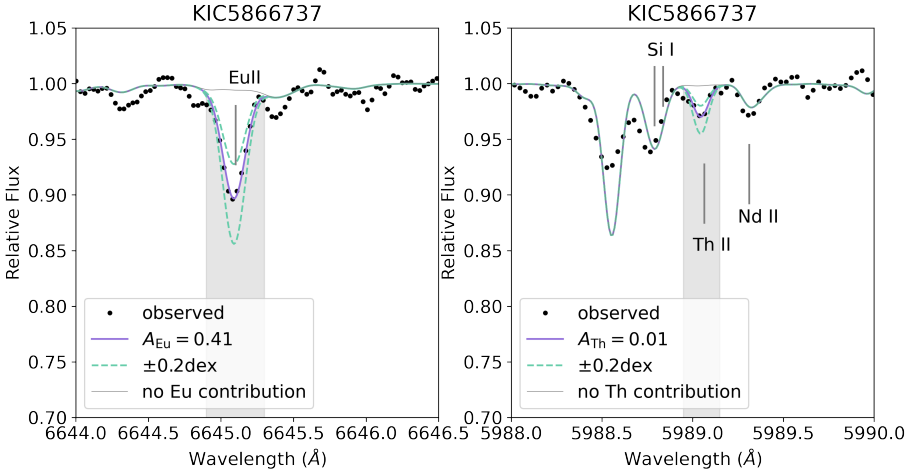
KIC5866737
EuII
Relative Flux
Wavelength (Å)
observed
$A_{Eu} = 0.41$
±0.2dex
no Eu contribution
KIC5866737
Si I
Nd II
Th II
observed
$A_{Th} = 0.01$
±0.2dex
no Th contribution

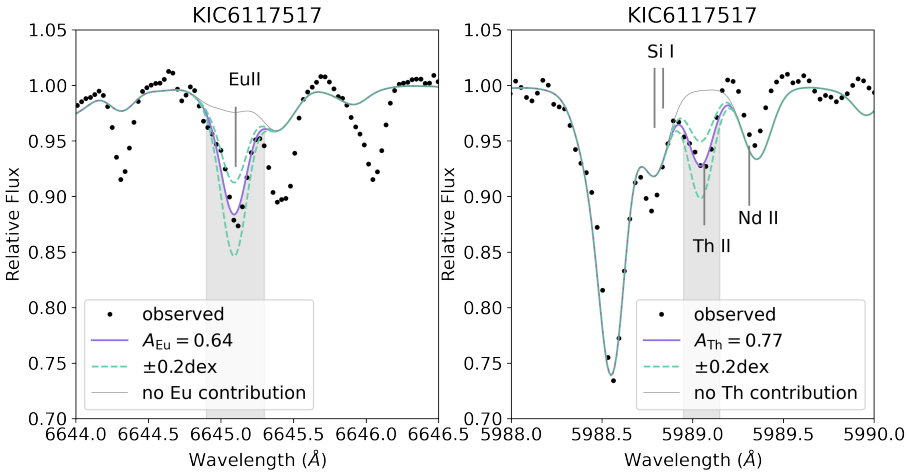
KIC6117517
EuII
Relative Flux
Wavelength (Å)
observed
$A_{Eu} = 0.64$
±0.2dex
no Eu contribution
KIC6117517
Si I
Nd II
Th II
observed
$A_{Th} = 0.77$
±0.2dex
no Th contribution

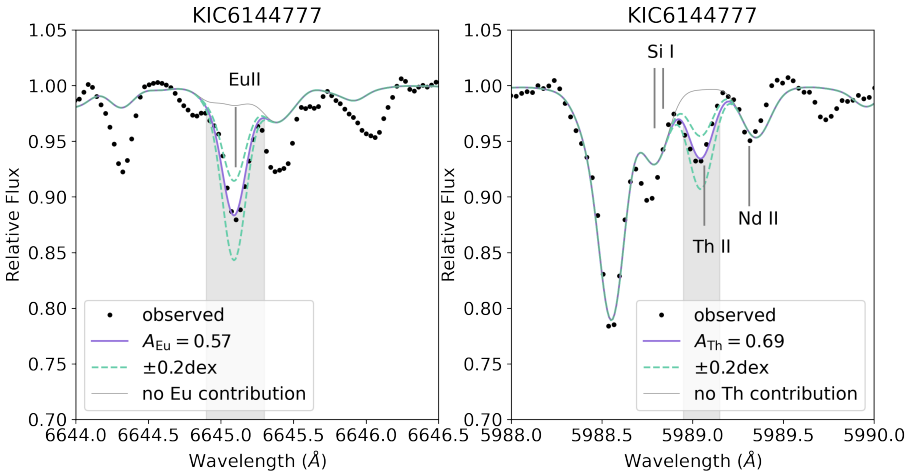
KIC6144777
EuII
Relative Flux
Wavelength (Å)
observed
$A_{Eu} = 0.57$
±0.2dex
no Eu contribution
KIC6144777
Si I
Nd II
Th II
$A_{Th} = 0.69$
no Th contribution

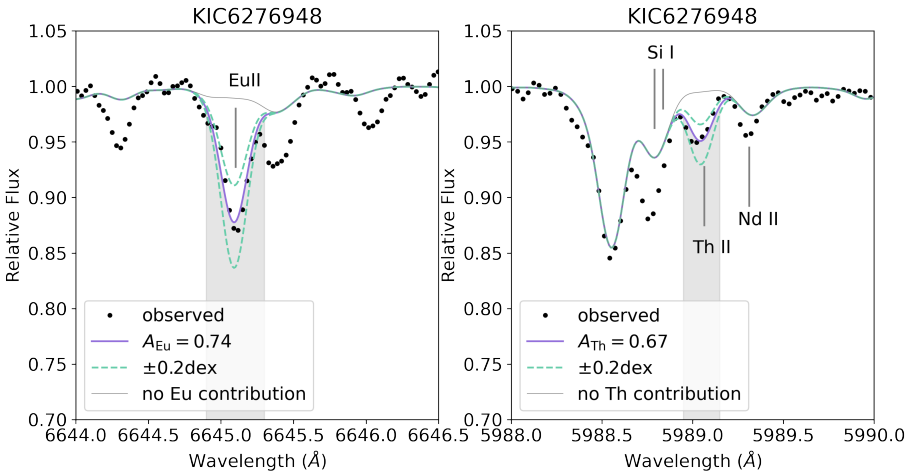
KIC6276948
EuII
Relative Flux
Wavelength (Å)
observed
$A_{Eu} = 0.74$
±0.2dex
no Eu contribution
KIC6276948
Si I
Nd II
Th II
$A_{Th} = 0.67$
no Th contribution

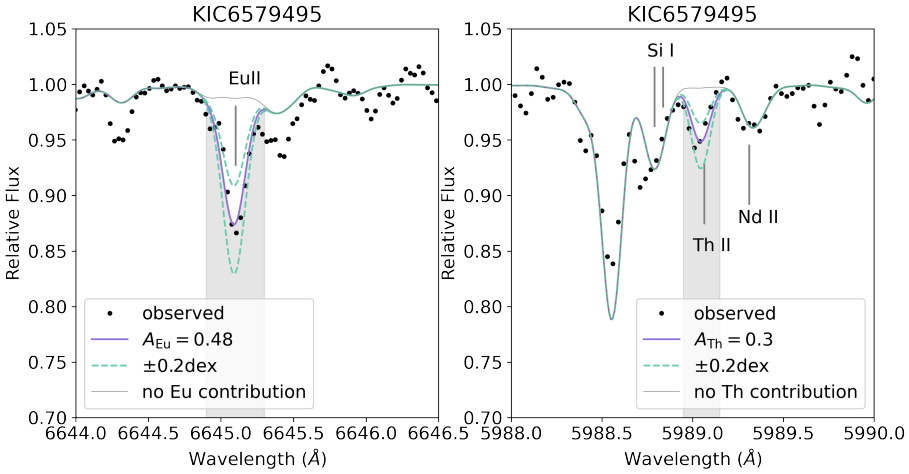
KIC6579495
EuII
Relative Flux
Wavelength (Å)
observed
$A_{Eu} = 0.48$
±0.2dex
no Eu contribution
KIC6579495
Si I
Nd II
Th II
$A_{Th} = 0.3$
no Th contribution

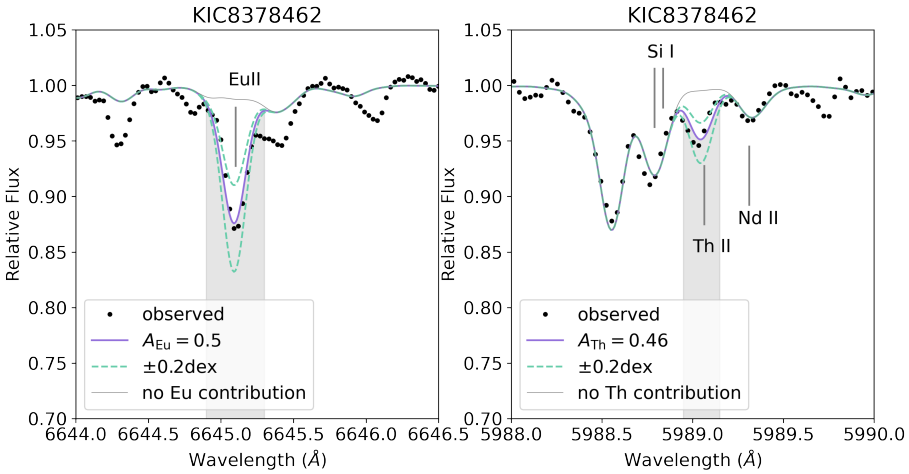
KIC8378462
EuII
observed
$A_{Eu} = 0.5$
±0.2dex
no Eu contribution
Relative Flux
Wavelength (Å)
KIC8378462
Si I
Nd II
Th II
observed
$A_{Th} = 0.46$
±0.2dex
no Th contribution
Relative Flux
Wavelength (Å)

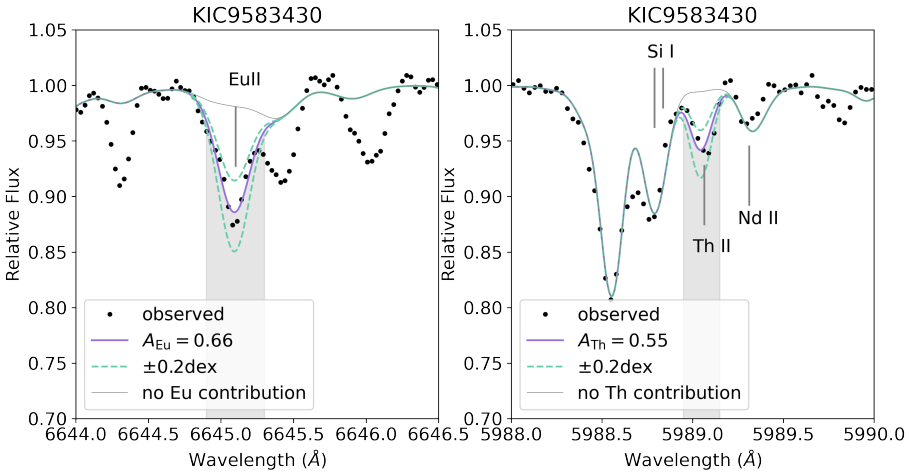
KIC9583430
EuII
observed
$A_{Eu} = 0.66$
±0.2dex
no Eu contribution
Relative Flux
Wavelength (Å)
KIC9583430
Si I
Nd II
Th II
observed
$A_{Th} = 0.55$
±0.2dex
no Th contribution
Relative Flux
Wavelength (Å)